MIC13 and SLP2 seed the assembly of MIC60-subcomplex to facilitate crista junction formation

Ritam Naha[1], Rebecca Strohm[1], Jennifer Urbach[1], Ilka Wittig[2, 3], Andreas S. Reichert[1], Arun Kumar Kondadi[1], Ruchika Anand[1*]

[1]Institute of Biochemistry and Molecular Biology I, Medical Faculty and University Hospital Duesseldorf, Heinrich Heine University Duesseldorf, Duesseldorf, Germany

[2]Functional Proteomics, Institute for Cardiovascular Physiology, Faculty of Medicine, Goethe-University, Frankfurt am Main, Germany.

[3]German Center of Cardiovascular Research (DZHK), Partner Site RheinMain, Frankfurt, Germany.

*Corresponding author: anand@hhu.de

Abstract

The MICOS complex subunit MIC13 is essential for mitochondrial cristae organization. Mutations in *MIC13* cause severe mitochondrial hepato-encephalopathy displaying defective cristae morphology and loss of the MIC10-subcomplex. Here we identified stomatin-like protein 2 (SLP2) as an interacting partner of MIC13 and decipher a critical role of SLP2 as an auxiliary MICOS subunit, modulating cristae morphology. SLP2 provides a large interaction hub for MICOS subunits and loss of SLP2 leads to drastic alterations in cristae morphology. Double deletion of SLP2 and MIC13 showed reduced assembly of core MICOS subunit, MIC60 into MICOS and dispersion of MIC60-specific puncta, demonstrating a critical role of SLP2-MIC13 in MICOS assembly and crista junction (CJ) formation. We further identified that the mitochondrial i-AAA protease YME1L in coordination either with MIC13 or SLP2 differentially regulates MICOS assembly pathways thereby interlinking MIC13-specific or scaffolding-specific role of SLP2 with quality control and assembly of the MICOS complex. YME1L-depletion in *MIC13* KO could restore MIC10-subcomplex and reform the nascent CJ. Taken together, we propose 'seeder' model for MICOS assembly and CJ formation, where SLP2-MIC13 seed the assembly of MIC60 into MICOS complex and promote the formation of CJ by regulating the quality and stability of MIC10-subcomplex.

52 **Introduction**

53 Mitochondria with their multifaceted roles are involved in many cellular functions, in addition to
54 energy conversion, namely calcium signalling, lipid metabolism, ROS production, amino acid
55 metabolism, iron-sulfur cluster synthesis and regulation of apoptosis (Monzel, Enríquez et al.,
56 2023). The inner membrane (IM) of mitochondria is versatile and adapts according to the
57 bioenergetic demands of the cell. Cristae are infoldings of the IM that provide the characteristic
58 wrinkled shape of IM and offer large surface area for housing electron transport chain (ETC)
59 complexes. The intricate three-dimensional (3D) arrangement of the IM was better illustrated
60 upon use of electron tomography techniques in 1990s leading to the proposal of crista junction
61 (CJ) model. CJs are small openings at the neck of individual cristae with a high inward-directed
62 curvature (Perkins, Renken et al., 1997). Due to their small diameter, CJs were proposed as a
63 diffusion barrier (Mannella, Lederer et al., 2013, Perkins et al., 1997) subdividing mitochondria
64 into various subcompartments and thus modulating several mitochondrial functions. CJ could
65 modulate lipid transfer and metabolite exchange in the mitochondria. The remodelling of CJ
66 during apoptosis lead to release of cytochrome *c* and initiation of apoptotic cascade (Scorrano,
67 Ashiya et al., 2002). However, how these intricate structures of cristae and CJ with steep
68 membrane curvatures are formed and remodelled remain elusive for decades . Several recent
69 findings provide insights on this very significant yet technically challenging question. MICOS
70 'mitochondrial contact site and cristae organising system' complex has emerged as a critical
71 player in formation of cristae and CJ (Anand, Reichert et al., 2021, Mukherjee, Ghosh et al.,
72 2021, Stephan, Brüser et al., 2020). Live-cell super-resolution nanoscopy showed that cristae
73 and CJs are highly dynamic and undergo cycles of fusion and fission at a timescale of seconds
74 in a MICOS-dependent manner (Kondadi, Anand et al., 2020). Mammalian MICOS complex
75 contains seven subunits that are further divided into two subcomplexes, the MIC60-
76 subcomplex (MIC60-MIC19-MIC25) and the MIC10-subcomplex (MIC10-MIC13-MIC26-
77 MIC27). Deletion of individual subunits of the MICOS complex causes aberrant cristae
78 morphology and accumulation of cristae stacks or concentric rings to a variable degree
79 (Kondadi et al., 2020, Stephan et al., 2020). MIC60 and MIC10 are the most important subunits

80 and are shown to harbour membrane bending activity (Barbot, Jans et al., 2015, Bock-
81 Bierbaum, Funck et al., 2022, Bohnert, Zerbes et al., 2015, Hessenberger, Zerbes et al., 2017,
82 Tarasenko, Barbot et al., 2017). MIC19 and MIC25 are coiled-coil helix coiled-coil helix (CHCH)
83 family proteins and important to assist MIC60 in the formation of CJs (An, Shi et al., 2012,
84 Sakowska, Jans et al., 2015). MIC13 is a small protein which is proposed as an essential
85 component for maintaining contact between the two MICOS subcomplexes (Anand, Strecker
86 et al., 2016, Guarani, McNeill et al., 2015, Urbach, Kondadi et al., 2021, Zerbes, van der Klei
87 et al., 2012). MIC26 and MIC27 are homologous proteins that belong to the apolipoprotein
88 family and required for cristae morphology, integrity of respiratory chain complexes and
89 cardiolipin levels (Anand, Kondadi et al., 2020). MIC27 has the ability to bind cardiolipin
90 (Weber, Koob et al., 2013). The interaction of the MICOS subunits with outer membrane (OM)
91 proteins SAMM50, metaxin1 (MTX1), metaxin2 (MTX2) and DNAJC11 forms a larger
92 'mitochondrial intermembrane space bridging' (MIB) complex that is responsible for formation
93 of contacts between IM and OM (Huynen, Muhlmeister et al., 2016, Tang, Zhang et al., 2020,
94 Xie, Marusich et al., 2007). Mutations in several MICOS subunits have been linked to various
95 human diseases but the pathobiology of mitochondrial diseases that are occurring due to the
96 non-ETC genes are not studied in detail. Mitochondrial diseases account of a large class of
97 inborn errors of metabolism with the prevalence rate of 1.6 in 5000 (Stenton & Prokisch, 2020).
98 Yet, no curative treatment is known. Mutations of *MIC60, MIC26 and MIC13* have been found
99 in several severe human diseases (Beninca, Zanette et al., 2021a, Guarani, Jardel et al., 2016,
100 Peifer-Weiß, Kurban et al., 2023, Russell, Whaley et al., 2019, Tsai, Lin et al., 2018, Zeharia,
101 Friedman et al., 2016). The question remains how cristae and CJs are formed and maintained
102 during the healthy or pathological conditions and how does specific MICOS subunit contribute
103 to these processes. In this study, we specifically focused on determining the molecular role of
104 MIC13 in cristae formation that could provide novel insights into the relevant pathobiology.

105 MIC13 is not well characterized and no homology was found with other protein families or
106 domains (Urbach et al., 2021). Loss of MIC13 causes concomitant total loss of MIC10, MIC26
107 and partial loss of MIC27, making it difficult to assign the specific phenotype to any of the

108 proteins involved (Anand et al., 2016, Guarani et al., 2015). We had reported two conserved
109 motifs, the 'GxxxG' and the 'WN' motif, in MIC13 that were important for its stability and function
110 (Urbach et al., 2021). Nevertheless, it is an important component of the MICOS complex and
111 mutations in *MIC13* are associated with severe form of mitochondrial hepato-encephalopathy
112 in children (Guarani et al., 2016, Russell et al., 2019, Zeharia et al., 2016). The patients die at
113 very early age ranging from a few months to 5 years. The pathology included multi-system
114 failure in brain, liver, kidney and heart (Godiker, Gruneberg et al., 2018, Guarani et al., 2016,
115 Russell et al., 2019, Zeharia et al., 2016). Neurological defects included cerebellar and optic
116 atrophy, acquired microcephaly and hypotonia. Most patients also showed clear signs of liver
117 disease accompanied by acute liver failure. Increased plasma levels of lactic acid, methionine,
118 tyrosine and kerbs cycle intermediates and increased excretion of 3-methylglutaconic acid was
119 reported. In all the cases documented, MIC13 levels were not detectable, indicating the
120 complete loss of MIC13 in these pathologies.

121 To identify the molecular role of MIC13, we set out to identify its interaction partners. Using
122 mass-spectrometry (MS) coupled with coimmunoprecipitation (co-ip) of MIC13, we detected
123 Stomatin-like protein 2 (SLP2) as one of the highly enriched proteins in MIC13 interactome. A
124 link to MICOS regulation or cristae morphogenesis has not been reported for SLP2. Here, we
125 identified SLP2 as an auxiliary subunit of MICOS. SLP2 provides a scaffold to form a large
126 interaction hub for all known MICOS subunits. Our results show a novel multi-layered role of
127 SLP2 in regulating MICOS assembly and cristae morphogenesis. SLP2 was specifically
128 required for the stability of MIC26 and its incorporation in the MICOS complex by regulating
129 YME1L-mediated MIC26 proteolysis. Moreover, the combined depletion of MIC13 and SLP2
130 accentuates defects in MIC60 assembly, emphasizing their collaborative roles in modulating
131 assembly kinetics and formation of MIC60 puncta. Next to novel roles of SLP2 and YME1L,
132 our study elucidates MIC13-specific role in MICOS assembly and cristae morphogenesis,
133 which is important for understanding the MIC13-associated pathophysiology. We further
134 introduce a 'seeder model' of MICOS assembly, wherein SLP2, along with an assembled
135 MIC10-subcomplex ('seeder' complex), facilitates the efficient incorporation 'seeding' of MIC60

136 into the holo-MICOS-MIB complex, ensuring mitochondrial integrity and formation of CJ and
137 contact between IM and OM.

138 **Results**

139 **Determining the MIC13 interactome**

140 To unravel the unidentified function of MIC13 in regulating MICOS and/or processes
141 independent of MICOS, we determined the MIC13 interactome. Isolated mitochondria from
142 Flp-In T-REx HEK293 cells were subjected to co-ip using agarose beads conjugated with
143 MIC13 antibody and the eluate fraction was analysed by MS to identify the proteins which were
144 specifically and significantly enriched in wild type cells compared to *MIC13* knockout (KO) cells.
145 The analysis led to identification of numerous proteins which constituted the interactome of
146 MIC13 in mammalian cells (Fig 1A, Supplementary Table 1). Many of the identified proteins
147 belonged to MICOS and MIB complex or their known interactors, which demonstrates the
148 specificity of the results and highlights the central role of MIC13 in MICOS-MIB regulation. We
149 also found SLP2 as a novel interaction partner which showed the highest fold enrichment in
150 significance upon statistical analysis (Fig 1A). SLP2 belongs to the SPFH (stomatin, prohibitin,
151 flotillin, HflC/K) superfamily of scaffolding proteins that can form microdomains in the
152 membrane by local lipid-protein interactions. SLP2 is an IM protein which can bind cardiolipin
153 (Christie, Lemke et al., 2011) and regulate many mitochondrial functions including biogenesis,
154 proteolysis and morphology during stress-induced mitochondrial hyperfusion (SIMH)
155 (Tondera, Grandemange et al., 2009). A direct role of SLP2 in regulation of MICOS-MIB and
156 cristae morphology has not yet been reported, prompting us to study this possibility in more
157 detail.

158 **SLP2 stably interacts with all MICOS subunits forming an interaction hub**

159 In order to validate the interaction between MIC13 and SLP2 (Fig 1A), the elution fraction from
160 the MIC13-FLAG co-ip was subjected to western blot (WBs) analysis and probed with an SLP2
161 antibody. The SLP2 band intensity was substantially higher in *MIC13* KO cells expressing
162 MIC13-FLAG compared to *MIC13* KO expressing an empty vector (EV) confirming the

163 interaction of MIC13 with SLP2 (Fig 1B). The absence of matrix protein HSP60 and ETC
164 protein Mt-CO2 in the elution fraction showed the specificity of the co-ip experiment (Fig 1B).
165 Of note, only a fraction of SLP2 interacted with MIC13 as other SLP2 remained in unbound
166 fraction compared to the positive interactor MIC27. Further, we tested the MIC13-SLP2
167 interaction using SLP2 as a bait in a co-ip experiment. For this, we generated *SLP2* KO cells
168 using CRISPR-Cas9 system and stably expressed SLP2 with a MYC tag at its C-terminus. Co-
169 ip was performed using MYC-trap agarose and the elution fraction was probed for antibodies
170 against SLP2, YME1L (known SLP2 interactor), all MICOS subunits, HSP60 and Mt-CO2 (as
171 negative controls). The presence of SLP2 and YME1L and the absence of HSP60 and Mt-CO2
172 in the elution fraction showed the specificity of the co-ip experiment (Fig 1C). All MICOS
173 subunits, and not only MIC13, were present in the elution fraction, showing that SLP2 can
174 directly or indirectly interact with all the MICOS subunits (Fig 1C). Proximity ligation assay
175 (PLA) can be used to determine and visualize the proximity (interaction) between two proteins
176 of interest. PLA using antibodies specific to SLP2 and individual MICOS subunits showed
177 numerous punctae in each cell which mark the interaction between SLP2 and individual
178 MICOS subunits compared to negative controls of Mt-CO2 & SLP2 or only SLP2 antibody (Fig
179 1D). Overall, several lines of evidence confirm the specific and reciprocal interaction of SLP2
180 with the MICOS complex.

181 Due to the known limitations of co-ip experiments, we cannot specify whether SLP2 interacts
182 individually with each MICOS subunit or whether there is a hierarchy in the interaction of
183 MICOS subunits with SLP2. To determine if the interaction between SLP2 and MICOS subunits
184 relies on any particular MICOS subunit, we decided to perform co-ip experiments in cells
185 deleted for individual MICOS subunit. We generated KO cells lacking individual MICOS
186 subunits (MIC10, MIC26, MIC27, MIC19, MIC25 and MIC60) in HEK293 cell lines and stably
187 expressed SLP2-Myc in these cell lines. As expected, the *MIC10* KO and *MIC13* KO cells
188 showed loss (or decrease) of all subunits of the MIC10-subcomplex (MIC10/13/26/27) while
189 KO of either *MIC26* or *MIC27* showed no drastic change in other MICOS subunits (Fig 2A).
190 Among the subunits of MIC60-subcomplex, *MIC60* KO cells showed a drastic decrease in

191 steady state levels of all other MICOS subunits, whereas *MIC19* KO cells showed reduced
192 MIC10, MIC60 and MIC13 (Fig 2B). *MIC25* KO cells showed no drastic defect in the levels of
193 other MICOS subunits (Fig 2B). Despite the known and observed loss of subunits of the
194 MIC10-subcomplex in *MIC10* KO and *MIC13* KO cells, we clearly observed that SLP2 still
195 interacts with YME1L, MIC19, MIC25 and MIC60 (Fig 2A). Similarly, SLP2 still interacted with
196 the remaining MICOS subunits in *MIC26* KO, *MIC27* KO and *MIC25* KO cells (Fig 2A, 2B). As
197 *MIC60* KO cells showed very low levels of all MICOS subunits in the input fraction, we included
198 an over-exposed blot in addition at the right (Fig 2B). This clearly showed that the remaining
199 MIC13, MIC26, MIC27 and MIC19 subunits in *MIC60* KO could still interact with SLP2 (Fig 2B).
200 Altogether, we conclude that SLP2 can stably interact with any remaining MICOS subunits
201 even when other individual MICOS subunits are lost.

202 We next performed a blue-native gel electrophoresis (BN-PAGE) to determine the high-
203 molecular weight complexes of SLP2 and MICOS. Normally, MICOS subunits are distributed
204 in two large complexes; a higher MICOS complex with around 2000 kDa size that is shown to
205 also include MIB subunits and the lower molecular weight MICOS complex with the size around
206 700 KDa (Anand et al., 2016). We found that SLP2 forms a high molecular weight complex
207 which runs parallel to the high-molecular weight MICOS complex at around 2000 kDa (Fig 2C).
208 This observation was also verified in the complexome profiling data from HEK293 cell (Anand
209 et al., 2016) which shows the co-clustering of SLP2 and MICOS subunits at the region of 2000
210 kDa (Supplementary Fig 1). Overall, these results show that SLP2 provides a scaffold to form
211 an interaction hub with the individual MICOS complex in the IM of mitochondria (Fig 2D).
212 Therefore, we suggest that SLP2 is an auxiliary subunit of MICOS complex.

213 **SLP2 and YME1L determine the stability of MIC26**

214 Next, we investigated the significance of the SLP2-MICOS interaction and asked whether loss
215 of SLP2 affects the steady state levels of MICOS subunits or the MICOS complex. Using WBs,
216 we analysed the levels of MICOS subunits in *SLP2* KO cells and found a drastic reduction in
217 the steady state levels of MIC26, while the steady state of other MICOS subunits were largely

218 unaltered (Fig 3A). The MICOS assembly using a BN-PAGE showed that MIC26 was sparsely
219 present in the MICOS complex as expected from the steady state levels, however the
220 incorporation of most other MICOS subunits into the MICOS complex appeared comparable
221 to WT (Fig 3B).

222 SLP2 interacts with mitochondrial proteases like YME1L, OMA1 and PARL and forms a large
223 hub of proteases within the IM known as SPY complex (Wai, Saita et al., 2016). We also
224 confirmed the interaction between SLP2 and YME1L (Fig 1C). However, previous study did
225 not identify any YME1L-specific substrate which is regulated by SLP2. Thus, we asked whether
226 the loss of MIC26 in *SLP2* KO cells occurs due to proteolysis via YME1L. To test this, we
227 depleted YME1L in *SLP2* KO cells using shRNA, and indeed found a rescue of the levels of
228 MIC26 in *SLP2* KO cells (Fig 3C). Overall, we found that SLP2 specifically protects MIC26
229 from proteolysis via YME1L in the MICOS complex (Fig 3D). We conclude that MIC26 is a
230 novel substrate of YME1L which is regulated by SLP2 and well in line with the regulation of
231 proteases by scaffolding proteins. Thus, we identified novel quality control axis of SLP2-
232 YME1L which specifically regulates the steady state levels of MIC26 in MICOS assembly.

233 **Loss of SLP2 impairs formation of cristae and crista junctions**

234 To determine how SLP2 interaction with MICOS subunits and reduction of MIC26 in *SLP2* KO
235 cells would influence cristae morphology, transmission electron microscopy (TEM) images
236 were acquired from *SLP2* KO cells. *SLP2* KO cells showed swollen cristae and significant
237 reduction in the number of cristae and CJs compared to the control cells (Fig 3E, F). To
238 determine whether cristae defects in *SLP2* KO occur due to reduced MIC26, we tried to
239 express MIC26 in *SLP2* KO cells. However even after multiple trials it was not possible to
240 obtain *SLP2* KO cells with stable MIC26 overexpression, perhaps due to the fact that MIC26
241 could not to be stabilized without SLP2 until YME1L is present. Therefore, we compared the
242 cristae morphology of *SLP2* KO with *MIC26* KO cells to determine if they show similar cristae
243 defects. *MIC26* KO cells showed branching of cristae which appear like a honeycomb, while
244 compared to wild-type cells the number of cristae were slightly reduced, yet the number of CJs

245 were comparable (Fig 3F). Overall, the cristae defect and the reduction in cristae number in
246 *SLP2* KO was severe compared to *MIC26* KO. This indicates that cristae defects in *SLP2* KO
247 cells do not only arise from loss of MIC26 but rather suggests that SLP2 has an additional role
248 in MICOS assembly and cristae morphology apart from maintaining the stability of MIC26.
249 Overall, we demonstrate that SLP2 is new auxiliary subunit of MICOS complex that could
250 modulate cristae and CJ.

251

252 **SLP2 and the MIC13 synergistically regulate MICOS assembly**

253 To determine whether there is any synergistic role of MIC13 and SLP2 in MICOS assembly
254 and cristae morphology, we deleted *SLP2* in *MIC13* KO to generate a double KO (DKO) of
255 *MIC13* and *SLP2*. Steady state levels of MICOS subunits were similar in single *MIC13* KO and
256 *MIC13-SLP2* DKO as the effect was due to MIC13 deficiency. However, MIC26 levels were
257 even more reduced in *MIC13-SLP2* DKO as compared to single *SLP2* KO or *MIC13* KO cells
258 (Fig 4A). The MICOS complex could not assemble fully and ran at a lower size in *MIC13* KO
259 cells due to loss of the MIC10-subcomplex as observed using MIC19 and MIC60 antibodies
260 (Fig 4B). Strikingly, the assembly of MIC19 and MIC60 into the MICOS complex was drastically
261 reduced in *MIC13-SLP2* DKO cells compared to *MIC13* KO. *MIC13-SLP2* DKO cells showed
262 a synergetic outcome on MICOS assembly with the reduced size of MICOS complex as seen
263 in *MIC13* KO cells as well as reduced incorporation of MIC60 and MIC19 into the MICOS
264 complex (Fig 4B). In sum, although single knockout cells lacking *SLP2* or *MIC13* were able to
265 manage MIC60-subcomplex assembly, the double deletion of SLP2 and MIC13 is detrimental
266 to MIC60-subcomplex assembly, showing a synergistic role of SLP2 and MIC13 in mediating
267 the assembly of the MIC60-subcomplex (Fig 4C). In order to determine the influence of such
268 a synergistic regulation of SLP2 and MIC13 on mitochondrial ultrastructure, we analysed the
269 cristae morphology in single and double KOs using TEM. *MIC13* KO displayed onion-like
270 cristae while *SLP2* KO displayed swollen cristae (Fig 4D), both having significantly reduced
271 number of cristae and CJs (Fig 4D, E). *MIC13-SLP2* DKO also had a similar severe phenotype

272 compared to *MIC13* KO cells with significantly reduced numbers of cristae and CJs. Hence,
273 we conclude that synergy between SLP2 and MIC13 is required for the assembly of MIC60-
274 subcomplex and formation of cristae and crista junction.

275 *MIC13-SLP2* DKO showed higher extent of mitochondrial fragmentation compared to either
276 single knockout cells (Fig 4F, G). This could be correlated with lower assembly of MIC60-
277 subcomplex as loss of MIC19 and MIC60 were previously shown to cause mitochondrial
278 fragmentation. SLP2 plays a role in stress-induced mitochondrial hyperfusion (SIMH) (Tondera
279 et al., 2009). To determine whether SLP2-MICOS interaction can influence SLP2-mediated
280 SIMH, mitochondrial morphology upon stress was analysed in single KOs and *MIC13-SLP2*
281 DKO. SIMH was induced by inhibition of protein synthesis using cycloheximide treatment,
282 which showed accumulation of hypertubular mitochondria in WT cells within 2 hours of
283 treatment (Supplementary Fig 2A, B). As expected, *SLP2* KO failed to show any response
284 upon SIMH. *MIC13* KO cells showed hyperfusion similar to WT cells, while *MIC13-SLP2* DKO
285 showed the response which was similar to single *SLP2* KO (Supplementary Fig 2A, B),
286 implying that SLP2-mediated SIMH occurs independent to its interaction with MICOS.

287 To understand whether SLP2 contributes towards the function of MIC13 to interact with the
288 MIC60-subcomplex and the MIC10-subcomplex, we checked for the interaction of MIC13 with
289 MICOS subunits in the presence and absence of SLP2 by expressing MIC13-FLAG in *MIC13*
290 KO or *MIC13-SLP2* DKO, respectively. MIC13 was able to interact with all MICOS subunits
291 even upon loss of SLP2, although the interaction with MIC26 was reduced due to MIC26
292 degradation in *SLP2* KO. This suggests that the MIC13-MICOS subunit interactions are
293 independent of SLP2. Additionally, we found a novel interaction of MIC13 with YME1L which
294 was also independent of SLP2 pointing towards a novel SLP2-independent MIC13-YME1L
295 axis in the IM (Supplementary Fig 3). In summary, we found that SLP2 and MIC13 regulate
296 the assembly of MIC60-subcomplex, which was independent to SLP2-mediated SIMH.

297 **SLP2 selectively regulates the assembly kinetics of MIC60-subcomplex**

298 To mechanistically dissect the role of SLP2 in regulating of MIC60 assembly, we decided to
299 apply the Tet-On system to reintroduce *MIC13* in a time-dependent manner and analyse re-
300 assembly of the MICOS complex over short time scales in *MIC13* KO and *MIC13-SLP2* DKO
301 cells. For this, we generated pLIX403-MIC13-FLAG and stably expressed it in the *MIC13* KO
302 and *MIC13-SLP2* DKO using the lentiviral transduction method. The addition of doxycycline
303 induces the expression of MIC13-FLAG in a time-dependent manner. After eight hours of
304 doxycycline induction, MIC13-FLAG started to express in both *MIC13* KO and *MIC13-SLP2*
305 DKO (Fig 5A). MIC13-FLAG was gradually expressed and incorporated into the MICOS
306 complex of both *MIC13* KO and *MIC13-SLP2* DKO cells as seen by BN-PAGE at different time
307 points after induction of protein expression (Fig 5B). Both MIC10 and MIC27 also progressively
308 assembled in the MICOS complex over time (Fig 5C). The appearance of the MIC10-
309 subcomplex as determined by probing the blots for MIC10 or MIC27 was more rapid and
310 efficient in *MIC13-SLP2* DKO cells compared to the *MIC13* KO cells. This could be due to
311 slightly higher expression of MIC13-FLAG in *MIC13-SLP2* DKO compared to the *MIC13* KO.
312 On the contrary, the incorporation of MIC60 into the MICOS complex was slower in *MIC13-*
313 *SLP2* DKO cells compared to the *MIC13* KO after induction of MIC13-FLAG. The arrows in the
314 Fig 4C show that MICOS size was recovering yet the amount of MIC60 in MICOS complex
315 took more time to recover (16 hours) in *MIC13-SLP2* DKO (Supplementary Fig 4A, B). Despite
316 the presence of the already assembled MIC10-subcomplex, it took more time for MIC60 to
317 assemble into MICOS complex when SLP2 was missing. The assembly kinetics of the MIC60-
318 subcomplex rather than the MIC10-subcomplex is dependent on SLP2 (Fig 5D), concluding
319 that SLP2 specifically regulates the incorporation of MIC60 into the MICOS complex.

320

321 **MIC13 stabilizes MIC10-subcomplex by regulation of YME1L-mediated proteolysis**

322 Next, we wanted to decipher the specific role of MIC13 in MIC13-SLP2 alliance for assembly
323 of MIC60-subcomplex. However, it has been difficult to identify the exact molecular role of

324 MIC13 because *MIC13* KO was always associated with loss of the MIC10-subcomplex making
325 it hard to differentiate whether the effects were arising due to MIC10 or MIC13 loss. Based on
326 two observations: a novel interaction between YME1L and MIC13 which is independent of
327 SLP2 (Supplementary Fig 3) and an increase in MIC10 levels upon the YME1L downregulation
328 in all the cell lines (Fig 3C), we hypothesized perhaps MIC10 degradation in *MIC13* KO could
329 be YME1L-mediated. We generated cell lines with stable expression of shRNA against YME1L
330 in WT, *SLP2* KO, *MIC13* KO and *MIC13-SLP2* DKO cell lines. Upon knockdown of YME1L,
331 the levels of MIC10 and MIC27 were not only enhanced in *MIC13* KO but also in *SLP2* KO and
332 *MIC13-SLP2* DKO cells showing that both MIC10 and MIC27 are novel YME1L substrates
333 which are regulated independent of SLP2 (Fig 6A). Next to the already described SLP2-
334 dependent YME1L proteolysis of MIC26 (Figure 4), here we identified a second quality control
335 axis of YME1L-mediated proteolysis of MIC10 and MIC27, which is independent to SLP2 but
336 rather dependent on MIC13, demonstrating an intricate mechanism of YME1L-dependent
337 quality control within the MICOS complex. Moreover, YME1L downregulation in *MIC13* KO
338 cells which restored MIC10 levels provides us an exclusive scenario to determine the specific
339 roles of MIC13 that are independent to MIC10. In *MIC13* KO cells, the MIC60-subcomplex
340 shows a lower molecular weight compared to the WT due to loss of the MIC10-subcomplex
341 (Fig 6B). We checked whether the restored levels of MIC10 using YME1L shRNA could
342 promote assembly of MIC10 with the MIC60-subcomplex in *MIC13* KO cells. Indeed, we
343 observed a MIC60 size shift in *MIC13* KO cells upon additional YME1L knockdown showing
344 that the MIC10-subcomplex can assemble with the MIC60-subcomplex despite the absence
345 of MIC13 (Fig 6B). This changes our view on MICOS assembly as it implies that MIC13 is not
346 required to bridge the MIC10- and MIC60-subcomplex, rather it plays an indispensable role in
347 stabilizing the MIC10-subcomplex and controls the quality of the MIC10-subcomplex via
348 YME1L-dependent proteolysis (Fig 6B).

349 **Stabilization of MIC10-subcomplex could partially promote CJ formation in *MIC13* KO**
350

351 To determine the interdependence between SLP2 and MIC13 for MIC60 assembly, we wanted
352 to check whether restoration of the MIC10-subcomplex in *MIC13-SLP2* DKO cells could
353 improve the MIC60 assembly into MICOS complex. Even though the steady state levels of
354 MIC60-subcomplex were not affected upon YME1L depletion, the assembly and the shift in
355 MIC60-subcomplex was partially restored in the *MIC13-SLP2* DKO background (Fig 6B). This
356 indicates that the assembled MIC10-subcomplex, in absence of SLP2, can partially provide a
357 'docking platform' for MIC60 and MIC19 to incorporate in the MICOS complex. The partial
358 restoration of MIC60-MIC19 assembly also reflected in the assembly of MIB complex protein
359 MTX1 (Fig 6B). MTX1 is a MIB subunit, together with SAMM50, it forms contact sites between
360 the IM and OM (Huynen et al., 2016). *MIC13-SLP2* DKO cells displayed a drastic reduction in
361 MTX1 assembly, which was restored upon depletion of YME1L (Fig 6B). Together, this data
362 points towards a larger role of SLP2-MIC13 axis in efficient assembly of the MIB complex in
363 association with MIC60-subcomplex.

364 To further validate the importance of the MIC10-subcomplex promoting the assembly of MIC60
365 into a functional MICOS and MIB complex, we investigated mitochondrial ultrastructure upon
366 depletion of YME1L in the single and DKO cell lines. Depletion of YME1L from *MIC13* KO and
367 *MIC13-SLP2* DKO cell lines led to a moderate beneficial effect on mitochondrial ultrastructure,
368 as the number of CJs were restored (Fig 6C, D). The images of a single mitochondrion showed
369 some cristae displaying intact CJ where it appeared that onion-shaped cristae unfurled to form
370 nascent CJ. Thus, indicating that stabilized MIC10-subcomplex can promote the formation of
371 nascent CJ in *MIC13* KO or *MIC13-SLP2* DKO (Fig 6C, D).

372

373 **SLP2 and MIC13 regulate the formation of MIC60 puncta in IM**

374 We show that MIC60 assembly into the MICOS complex was reduced in *MIC13-SLP2* DKO
375 cells, while the steady state levels of MIC60 was comparable to controls. Therefore, we wanted
376 to determine the status of MIC60 distribution in the IM in these KO cell lines. Using super-
377 resolution stimulated emission depletion (STED) nanoscopy, the distribution of MIC60 in the

378 IM was marked with MIC60-specific antibodies. MIC60 showed punctate pattern with the rail-
379 like arrangement, which is consistent with previous publications (Jans, Wurm et al., 2013,
380 Kondadi et al., 2020, Stoldt, Stephan et al., 2019). This pattern of MIC60 staining resembles
381 the arrangement of CJs in the mitochondria. MIC60 staining in the *MIC13-SLP2* DKO was
382 remarkably different, compared to the WT cells, with less punctate structures and diffuse
383 staining pattern evenly spread along the IBM. The staining of MIC60 in single *MIC13* KO and
384 *SLP2* KO was also perturbed and the rail-like pattern was less prominent as the MIC60 spots
385 were also equally distributed within the mitochondria (Fig 7A). MIC60 could be present on the
386 inner cristae stacks that are accumulated in *MIC13* KO and *SLP2* KO. Even though the single
387 KOs could manage MIC60 puncta formation, the combined loss of SLP2 and MIC13 was
388 detrimental to MIC60 puncta formation, demonstrating a critical role of SLP2 in dictating
389 formation of MIC60 puncta perhaps by facilitating the formation of a conducive lipid
390 microenvironment. Stomatins are shown to create the microdomains in the lipid-bilayer.
391 Therefore, we propose that SLP2-MIC10-subcomplex acts as 'seeder' for the formation of
392 MIC60 puncta in IM and thereby promote formation of CJ.

393 Overall based on our results, we propose a 'seeder' model for the assembly of MICOS complex
394 which shows interdependence of the assembly of MIC60-subcomplex and the MIC10-
395 subcomplex on each other and on the scaffolding protein, SLP2 (Fig 7B). The arrangement of
396 the MIC60 was dispersed upon loss of both SLP2 and MIC13. The preliminary MIC60-
397 subcomplex is dispersed in the IM and unable to contact MIB components. The MIC10-
398 subcomplex is intricately stabilized and assembled by two differentially regulated quality
399 control axes dependent on YME1L. The 'seeder' complex is formed by association of SLP2
400 and MIC10-subcomplex, which provides a docking platform for further assembly of MIC60-
401 subcomplex into holo-MICOS complex and MIB complex. This is shown by formation of MIC60-
402 specific puncta in the presence of both SLP2 and MIC13 and leading to reattachment of the
403 cristae stacks to IM and formation of nascent CJ as well contact site between IM and OM. The
404 concomitant reappearance of CJ upon stabilization of MIC10-subcomplex provides
405 mechanistic insights for formation of nascent CJ.

406 **Discussion**

407 MIC13 being an integral component of the mitochondrial IM has been vital for cristae
408 morphogenesis and loss of MIC13 leads to severe mitochondrial hepato-encephalopathy.
409 Although previous research has extensively shown the consequence upon MIC13 depletion,
410 molecular mechanisms leading to the phenotypes are largely unknown. Here we determined
411 the interactome of MIC13 to obtain novel insights about the unidentified molecular role of
412 MIC13. The interactome data mostly contained proteins belonging to MICOS-MIB complex or
413 the known interactor of these complexes, implying a crucial role of MIC13 in MICOS regulation.
414 Among few novel interactors, SLP2 was one of the most highly enriched protein. SLP2 belongs
415 to the SPFH (stomatin, prohibitin, flotillin, HfLC/K) superfamily which is composed of
416 scaffolding proteins that can locally define the protein and lipid configuration of a cellular
417 membrane (Wai et al., 2016). Though an interesting possibility, a direct role of SLP2 in MICOS
418 assembly and cristae dynamics was not reported earlier. Using KOs of individual MICOS
419 subunits and stable overexpression cell lines, we determined that SLP2 not only interacts with
420 MIC13 but also with each MICOS subunit and forms a large interaction hub of SLP2-MICOS
421 in the mitochondrial IM. Our results show novel multi-layered roles of SLP2 in regulating the
422 MICOS assembly and CJ formation. SLP2 was identified as a new cristae and CJ modulator
423 as loss of SLP2 leads to defects in cristae and CJ morphology. Based on these results, we
424 propose SLP2 as an auxiliary subunit of MICOS. SLP2 was required for stability of MIC26 and
425 its assembly into MICOS complex. It protects MIC26 from YME1L-mediated proteolysis. SLP2
426 was earlier shown to form proteolytic hub with mitochondrial proteases PARL, YME1L and
427 perhaps OMA1 known as SPY complex. However, no earlier known substrates of YME1L were
428 shown to be regulated by the SPY complex (Wai et al., 2016). We show here that MIC26 is a
429 novel substrate of YME1L which is specifically regulated by the SLP2-YME1L axis. Recently,
430 we have reported a pathological mutation in *MIC26* that causes lethal mitochondrial disease
431 with progeria-like phenotypes (Peifer-Weiß et al., 2023). This MIC26 variant with loss of the
432 last twenty amino acids at the C-terminus is prone to faster degradation such that the mutant
433 behaves like a loss-of-function variant. Perhaps MIC26 degradation in patient cells is the

434 consequence of enhanced SLP2-YME1L-mediated proteolysis. *MIC26* mutations were also
435 associated with recessive mitochondrial myopathy, lactic acidosis, cognitive impairment and
436 autistic features (Beninca, Zanette et al., 2021b). Further study of SLP2-YME1L axis to
437 regulate MIC26 could provide the patho-mechanisms in MIC26-associated pathologies.

438 Although SLP2 showed a specific regulation of MIC26, our interaction data and the fact that
439 *SLP2* KO shows more severe cristae defects compared to *MIC26* KO pointed towards possible
440 broader roles of SLP2 in MICOS assembly and cristae architecture. Peculiarly, the DKO of
441 *MIC13* and *SLP2* showed more additive defects compared to each single KO with respect to
442 the MIC60 assembly into the MICOS complex. This indicated that MIC13 and SLP2 function
443 in unison to regulate the incorporation of MIC60 into the MICOS complex. The time-dependent
444 restoration of MIC13 in *MIC13-SLP2* DKO cells showed a considerably slower kinetics of the
445 assembly of MIC60 into MICOS complex compared to *MIC13* KO. This demonstrated a critical
446 role of SLP2 in regulating the kinetics of MIC60-subcomplex assembly and CJ formation.

447 To dissect the specific role of MIC13 in the regulation of MIC60 assembly in SLP2-MIC13 axis,
448 we wanted to differentiate whether the phenotypes arise from MIC10 or MIC13 as *MIC13* KO
449 is always associated with loss of MIC10-subcomplex. Based on our observations that MIC13
450 interacts with YME1L and MIC10 levels are enhanced in YME1L downregulation, we checked
451 whether MIC10 levels are regulated by YME1L in *MIC13* KO cells. The downregulation of
452 YME1L in *MIC13* KO could not only restore the steady state levels of MIC10 but also its
453 incorporation into the MICOS complex. Since MIC10 could be integrated in MICOS complex
454 in absence of MIC13, we conclude that while MIC13 in principle is dispensable for bridging
455 MIC10- and MIC60-subcomplexes, it rather plays an important role in stabilizing the MIC10-
456 subcomplex via inhibiting YME1L-specific proteolysis. The presence of nascent CJ upon
457 depletion of YME1L in *MIC13* KO showed that the assembled MIC10-subcomplex could form
458 CJ even in the absence of MIC13. The cristae in this scenario appeared as if the onion-like
459 cristae of *MIC13* KO unfurled and reattached to IM to form nascent CJ, providing a model for
460 CJ formation. MIC10 is known to oligomerize in a wedge-like shape that causes membrane

461 bending and CJ formation (Barbot et al., 2015, Bohnert et al., 2015). However, here question
462 remains whether this CJ restoration is sufficient to restore MIC13-specific mitochondrial
463 defects or the associated pathology. We also observe that MIC27 showed a band at a lower
464 apparent molecular weight in *MIC13* KO. The identity of the lower MIC27 is not yet known but
465 it was interesting to note that conversion of MIC27 to a lower size was MIC13-dependent and
466 was not influenced by YME1L depletion. This is because even when the steady state levels of
467 MIC27 was restored upon downregulation of YME1L in *MIC13* KO, the status of the MIC27
468 band size was not restored. The YME1L-dependent restoration of MIC10 presents a new tool
469 to distinguish the MIC13-specific functions, which has direct implications in study of the MIC13-
470 associated disease mechanism and in development of future therapeutics.

471 Using YME1L as a tool, we restored the MIC10 levels in *MIC13-SLP2* DKO and checked for
472 MIC60 incorporation into MICOS complex. Here, we found that restoration of MIC10 could
473 partially restore the incorporation of MIC60 into the MICOS complex in the *MIC13-SLP2* DKOs.
474 This showed an interdependence of SLP2 and MIC10-subcomplex for the MIC60 assembly,
475 where SLP2 and the MIC10-subcomplex that is stabilized by MIC13 act as a 'seeder' for
476 incorporation of MIC60 into the holo-MICOS complex. We termed SLP2-MIC10-subcomplex
477 as a 'seeder' complex. In agreement, the super-resolution STED nanoscopy showed a
478 dispersed arrangement of MIC60 in the IM in *MIC13-SLP2* DKO compared to a normal rail-like
479 punctate arrangement in the control cells. This implies that MIC60 in the absence of SLP2 and
480 MIC13 could not be confined to MICOS puncta but rather remains dispersed. SLP2 and MIC13
481 direct the site for MIC60 puncta formation and thereby the CJ formation. Perhaps SLP2 role is
482 to generate special lipid environment for efficient MIC60-subcomplex assembly and its
483 association to its docking partner, MIC10-subcomplex. In conclusion, both SLP2 and MIC13
484 work together to generate a conducive environment for efficient incorporation of MIC60 into
485 MICOS-MIB complex and thereby CJ formation.

486 Initially it has been thought that MICOS assembly follows a hierarchy where MIC60
487 subcomplex assembly happens prior to MIC10-subcomplex and MIC60 act as a master

488 regulator (Ott, Dorsch et al., 2015, Zerbes, Hoss et al., 2016). However, our results show an
489 interdependence between these two steps: wherein kinetics of MICOS subcomplex assembly
490 progresses in an interdependent manner, concurrently SLP2 promotes the efficient assembly
491 of MIC60-subcomplex. Hence, we propose the 'seeder' model for the assembly of the MICOS-
492 MIB complex. We identified two differentially regulated quality control processes, SLP2-YME1L
493 and the MIC13-YME1L axis, that determine the stability and assembly of MIC10-subcomplex.
494 Once the MIC10-subcomplex is stabilized, the collaboration between MIC10-subcomplex and
495 the auxiliary MICOS subunit SLP2 (seeder complex) acts as a 'seeder' for formation of MIC60-
496 specific puncta and thereby incorporation of MIC60-subcomplex into MICOS-MIB complex.
497 Therefore, the seeder complex dictates the site for formation of MIC60 puncta and hence the
498 morphogenesis of CJ and contact site between the IM and OM.

499 The function of CJ and contact sites are not fully understood. Defects in the MICOS subunits
500 are shown to affect several important cellular functions including import of mitochondrial
501 protein, biogenesis and transfer of phospholipids, mtDNA organization, apoptosis, mitophagy,
502 mitochondrial transport, mitochondrial translation, mitochondrial morphology and inflammation
503 (Anand et al., 2021). The role of SLP2 and newly identified quality control axes in process of
504 MICOS-MIB could provide new insights into many of these cellular processes in future studies.

505 The quality control of MICOS assembly is intricately regulated by YME1L-mediated proteolysis
506 at different steps. SLP2-YME1L axis regulates the MIC26 stability and function. A Novel
507 MIC13-YME1L axis reported here, on the other hand, regulates MIC10, MIC26 and MIC27
508 levels independent of SLP2. MIC60 and SAMM50 were also proteolytic substrates of YME1L
509 during *MIC19* downregulation (Li, Ruan et al., 2016, Tang et al., 2020) showing the complexity
510 of regulation of MICOS assembly. Another IM protease, OMA1 also associates with the MICOS
511 complex (Viana, Levytskyy et al., 2021) and proteolytically regulates MIC19 assembly in the
512 MIB complex (Tang et al., 2020). Overall, our study deciphers a novel quality control
513 mechanism in regulating MICOS and MIB assembly and expands our understanding on the
514 factors regulating cristae morphogenesis.

515

516 **Materials and methods**

517 **Cell culture**

518 Flp-In T-REx HEK293 and HeLa cells were cultured in Dulbecco's modified Eagle medium
519 (DMEM) with 1g/L glucose and sodium pyruvate (PAN-Biotech, P04-01500) supplemented
520 with 1% stable glutamine (P04-82100), 1% penic illin-streptomycin (Sigma-Aldrich, P4333-
521 100ml), 10% fetal bovine serum (FBS) (Capricorn Scientific, FBS-11A). Plat-E and HEK293FT
522 cells were cultured in DMEM high glucose medium (PAN-Biotech, P04-03500) supplemented
523 with 10%FBS, 1% stable glutamine, 1% sodium pyruvate (Gibco, 11360070). GIPZ-Control-
524 Flp-In T-REx HEK293 and GIPZ-YME1LshRNA- Flp-In T-REx HEK293 cells were cultured in
525 DMEM 1g/L glucose medium containing sodium pyruvate supplemented with 1% stable
526 glutamine, 10% FBS, 1% penicillin-streptomycin and 1% Non-Essential Amino Acids Solution
527 (NEAA) (PAN-Biotech, P08-32100). All cells were cultured in at 37°C with 5% CO_2. All cell line
528 generated are listed in Supplementary Table 2.

529 **Co-immunoprecipitation coupled mass spectrometry**

530 Co-IP was performed with Protein A Sepharose CL-4B beads (Invitrogen, 101041) and affinity
531 purified MIC13 antibody was linked to the beads. Isolated mitochondria from Flp-In T-REx
532 HEK293 WT or *MIC13* KO were solubilized with isotonic buffer (150 mM NaCl, 10 mM Tris/HCl
533 (pH 7.5), 5 mM EDTA, 1x protease inhibitor cocktail) supplemented with 5 µl of 10% Digitonin
534 (2g/g of protein) and added to the beads with subsequent incubation in 4°C under rotation
535 conditions. Beads were washed several times, transferred into a new tube in 10mM Tris, pH
536 7.4. Beads were resuspended in 50 µl 6M GdmCl, 50 mM Tris/HCl, pH 8.5 and incubated at
537 95°C for 5 min. Sample were diluted with 25 mM Tris/HCl, pH 8.5, 10% acetonitrile to obtain a
538 final GdmCl concentration of 0.6 M. Proteins were digested with 1 µg Trypsin (sequencing
539 grade, Promega) overnight at 37°C under gentle agitation. Digestion was stopped by adding
540 trifluoroacetic acid to a final concentration of 0.5%. Peptides were loaded on multi-stop-and-
541 go tip (StageTip) containing six C18 discs. Purification and elution of peptides was performed

542 as described in Kulak, *et al* (Kulak, Pichler et al., 2014). Peptides were eluted in wells of
543 microtiter plates and peptides were dried and resolved in 1% acetonitrile, 0.1 % formic acid.
544 Liquid chromatography/ mass spectrometry (LC/MS) was performed on Thermo Scientific™ Q
545 Exactive Plus equipped with an ultra-high performance liquid chromatography unit (Thermo
546 Scientific Dionex Ultimate 3000) and a Nanospray Flex Ion-Source (Thermo Scientific).
547 Peptides were loaded on a C18 reversed-phase precolumn (Thermo Scientific) followed by
548 separation on a with 2.4 µm Reprosil C18 resin (Dr. Maisch GmbH) in-house packed picotip
549 emitter tip (diameter 100 µm, 30 cm long from New Objectives) using an gradient from mobile
550 phase A (4% acetonitrile, 0.1% formic acid) to 60 % mobile phase B (99% acetonitrile, 0.1%
551 formic acid) for 90 min with a flow rate 350 nl/min. MS data were recorded by data dependent
552 acquisition Top10 method selecting the most abundant precursor ions in positive mode for
553 HCD fragmentation. Lock mass option (Olsen, Godoy et al., 2005) was enabled to ensure high
554 mass accuracy between multiple runs. The Full MS scan range was 300 to 2000 m/z with
555 resolution of 70000, and an automatic gain control (AGC) value of 3*106 total ion counts with
556 a maxim al ion injection time of 160 ms. Only higher charged ions (2+) were selected for
557 MS/MS scans with a resolution of 17500, an isolation window of 2 m/z and an automatic gain
558 control value set to 105 ions with a maximal ion injection time of 150 ms. Selected ions were
559 excluded in a time frame of 30s following fragmentation event. Fullscan data were acquired in
560 profile and fragments in centroid mode by Xcalibur software. For data analysis MaxQuant
561 1.6.1.0 (Cox and Mann, 2008, Nat. Biotechnology), Perseus 1.5.6.0 (Tyranova et al 2016) and
562 Excel (Microsoft Office 2013) were used. N-terminal acetylation (+42.01) and oxidation of
563 methionine (+15.99) were selected as variable modifications and carbamidomethylation
564 (+57.02) on cysteines as a fixed modification. The human reference proteome set (Uniprot,
565 July 2017, 701567 entries) was used to identify peptides and proteins with a false discovery
566 rate (FDR) less than 1%. Minimal ratio count for label-free quantification (LFQ) was 1. Reverse
567 identifications and common contaminants were removed and the data-set was reduced to
568 proteins that were identified in at least 5 of 7 samples in one experimental group. Missing LFQ
569 or IBAQ values were replaced by random background values. Significant interacting proteins

570 were determined by permutation-based false discovery rate (FDR) calculation and students T-
571 Test. The mass spectrometry proteomics data have been deposited to the ProteomeXchange
572 Consortium via the PRIDE [1] partner repository with the dataset identifier PXD044968.

573 **Proximity ligation assay**

574 PLA was carried out with Duolink® In Situ Red Starter Kit Mouse/Rabbit (Sigma-Aldrich,
575 DUO92101-1KT) following manufacturer's protocol with minor modifications. Briefly, HeLa
576 cells were fixed using 4% paraformaldehyde (Sigma-Aldrich, P6148) for 20 mins in room
577 temperature and washed with PBS 3x with subsequent permeabilization with 0.15% Triton X-
578 100 (Sigma-Aldrich, T8787-100ML) in room temperature for 15 mins followed by PBS wash.
579 Permeabilized cells were blocked with blocking solution (provided in kit) for 1 hour in 37°C.
580 Blocking solution was removed and primary antibodies with 1:100 dilution ratio was added to
581 the samples and incubation was carried out at 37°C for 2 hours. Following primary antibodies
582 were used: MIC10 (Abcam, 84969), MIC13 (custom made by Pineda (Berlin) against human
583 MIC13 peptide CKAREYSKEGWEYVKARTK), MIC19 (Proteintech, 25625-1-AP), MIC25
584 (Proteintech, 20639-1-AP), MIC26 (Thermofisher Scientific, MA5-15493), MIC27 (Sigma-
585 Aldrich, HPA000612-100UL), MIC60 (Abcam, ab110329), SLP2 (Abcam, ab102051), SLP2
586 (OriGene, TA808240), Mt-CO2 (Abcam, ab110258). Subsequent ligation of PLA probes and
587 amplification of circular DNA probes was carried out following manufacturer's protocol. PLA
588 signals were visualized in PerkinElmer spinning disc confocal microscope equipped with a 60×
589 oil objective.

590 **CRISPR-Cas9 knockout generation**

591 CRISPR-Cas9 double nickase plasmid (Santa Cruz Biotechnology, SLP2: sc-403638-NIC,
592 MIC26: sc-413137-NIC, MIC60: sc-403617-NIC, MIC25: sc-413621-NIC, MIC19: sc-408682-
593 NIC, MIC10: sc-417564-NIC, MIC27: sc-414464-NIC) was transfected with GeneJuice (Sigma-
594 Aldrich, 70967-3) in Flp-In T-REx HEK293 WT, *MIC13* KO parental lines to generate KO and
595 double KO cell lines. Briefly, cell lines were transfected at 60-70% confluency with 1 µg of
596 double nickase plasmid and incubated for 48 hours followed by 2.5 µg/ml puromycin selection

597 for 24 hours with subsequent single cell sorting based on green florescent protein (GFP)
598 expression using flow cytometry in 96 well plate. Cells were incubated and upon visible
599 colonies, cells were sub-cultured and KO screen was performed with western blotting. Cell
600 lines showing no immune reactivity to respective antibodies were termed as KOs or double
601 KOs.

602 **Molecular cloning**

603 Human SLP2-HA ORF (Sino Biologicals, HG16147-CY) was cloned into pMSCVpuro vector
604 using Gibson assembly cloning kit (NEB, E2611L), following manufacturer's protocol. HA tag
605 was replaced with MYC tag with Site Directed and Ligation Independent Mutagenesis (SLIM)
606 (Chiu, Tillett et al., 2008) to generate pMSCV-SLP2-MYC. Human MIC13-Flag from pMSCV
607 puro MIC13-FLAG (Urbach et al., 2021) was cloned into pLIX403 (Addgene, 41395) with
608 Gibson assembly following manufacturers protocol. Primer sequences for Gibson assembly
609 and SLIM are provided in Supplementary Table 3.

610 **Generation of stable cell lines**

611 For retroviral transduction, Plat-E cells were transfected with 1 µg of pMSCV-MIC13Flag or
612 pMSCV-SLP2MYC and 1 µg of pVSV-G with 3.5 µL of GeneJuice per wells of 6-well plate.
613 After 72 hours incubation, viral supernatant was added to the target cells. Media was replaced
614 with puromycin containing media (2.5 µg/ml) 48 hours of transduction. Puromycin selection
615 was carried out for 2 weeks and successful expression of exogenous protein was validated
616 with western blot. For lentiviral transduction, HEK293FT cells were transfected with 1ug of
617 pLIX403 EV or pLIX403-MIC13-Flag or pGIPZ-non-silencing-Control-shRNA (Horizon
618 Discovery, RHS4346) or pGIPZ-YME1L-shRNA (Horizon Discovery, RHS4430-200157017,
619 RHS4430-200215861, RHS4430-200221198, RHS4430-200268420, RHS4430-200273633,
620 RHS4430-200280144) along with 1µg of psPAX2 (Addgene, 12260) and pMD2.G (Addgene,
621 12259) was transfected using GeneJuice. 72 hours post transfection, viral supernatant was
622 collected and added on target cell lines. Media was replaced with puromycin (2.5 µg/ml)

623 containing media and selection was carried out for about 2 weeks. Successful exogenous
624 protein expression or knockdown was confirmed with western blotting.

625 **SDS PAGE and Western blot**

626 Cells were grown in 6-well dishes and harvested with cold PBS upon 70-90% confluency
627 followed by protein extraction by RIPA lysis. Protein concentration was determined by Lowry
628 method (Bio-Rad, 5000113, 5000114, 5000115) and samples were prepared using Laemmli
629 loading buffer. Proteins were separated using 10% or 15% SDS-PAGE with subsequent
630 transfer on nitrocellulose membrane (Amersham, 10600004) followed by 1 hour of blocking
631 using 5% skimmed milk (Carlroth, 68514-61-4). Membranes were incubated overnight in 4°C
632 under shaking conditions in primary antibodies: MIC10 (Abcam, 84969), MIC13 (custom made
633 by Pineda (Berlin) against human MIC13 peptide CKAREYSKEGWEYVKARTK), MIC19
634 (Proteintech, 25625-1-AP), MIC25 (Proteintech, 20639-1-AP), MIC26 (Thermofisher Scientific,
635 MA5-15493), MIC27 (Sigma-Aldrich, HPA000612-100UL), MIC60 (Abcam, ab110329), SLP2
636 (Abcam, ab102051), beta-tubulin (Cell Signalling Technology, 2128S), HSP60 (sigma,
637 SAB4501464), Mt-CO2 (Abcam, ab110258), YME1L (Proteintech, 11510-1-AP), MTX1
638 (Abcam, ab233205). Following primary antibody incubation, membranes were washed in
639 TBST and probed with Goat anti-mouse IgG HRP-conjugated antibody (Abcam, ab97023) or
640 goat anti-rabbit IgG HRP-conjugated antibody (Dianova, 111-035-144). Chemiluminescent
641 signal was recorded with VILBER LOURMAT Fusion SL (Peqlab) and quantification was
642 performed with ImageJ.

643 **Mitochondria Isolation**

644 Cells were grown in 15 cm dishes and scrapped in cold PBS and pelleted at 500g for 5 mins.
645 Cell pellets were resuspended in isotonic buffer (220 mM mannitol, 70 mM sucrose, 1 mM
646 EDTA, 20 mM HEPES (pH 7.5) and 1 × protease inhibitor cocktail (Sigma-Aldrich,
647 05056489001)) with 0.1% bovine serum albumin (BSA) (Pan-Biotech, P06-1394100). Cells
648 were mechanically homogenized using syringe with 26G cannula for 15 strokes. Cell
649 homogenate was centrifuged at 1000g for 10 mins, supernatant was collected in fresh tube

650 and further centrifuged at 10,000g for 10 mins at 4°C to obtain crude mitochondrial fractions.
651 Crude mitochondrial pellets were resuspended in isotonic buffer and Lowry assay was
652 performed to determine the concentration. Crude mitochondrial fractions were aliquoted,
653 centrifuged at 10,000g for 5 mins and pellets were resuspended in freezing buffer (300 M
654 trehalose, 10 mM KCl, 1 mM EDTA, 10 mM HEPES and 0.1% BSA) and stored in -80°C until
655 further processing.

656 **Co-immunoprecipitation**

657 Mitochondrial aliquots of 500 µg were pelleted by centrifugation and re-suspended in isotonic
658 buffer (150 mM NaCl, 10 mM Tris/HCl (pH 7.5), 5 mM EDTA, 1x protease inhibitor cocktail)
659 with 10 µl of 10% Digitonin (2g/g of protein) and solubilized for 10 mins on ice. Solubilized
660 proteins were centrifuged at 21,000g for 20 mins and 10% of the supernatant was separated
661 as input fraction. Remaining supernatant were incubated with anti-Flag M2 affinity beads
662 (Sigma) or MYC-Trap agarose beads (ChromTech) overnight in 4°C under rotation. Beads
663 were centrifuged at 3700g for 1 min at 4°C and 300 µl supernatant was stored as unbound
664 fraction. Beads were further washed (4x) with isotonic buffer with 0.01% digitonin. Proteins
665 were eluted with Laemmli buffer without beta-mercaptoethanol at 65°C for 10 min with
666 subsequent addition of 1 µl beta-mercaptoethanol and subjected to SDS-PAGE with
667 subsequent western blotting.

668 **Visualization of native protein complexes with blue native PAGE**

669 Mitochondrial aliquots of 150ug were centrifuged and pellets were resuspended in 15 µl of
670 solubilization buffer (50 mM NaCl, 2 mM aminohexanoic acid, 50 mM imidazole/HCl pH 7, 1
671 mM EDTA, protease inhibitor cocktail) with 3 µl of 10% digitonin (2g/g of protein) and incubated
672 on ice for 10 mins. Samples were centrifuged at 21,000g for 10 mins at 4°C and supernatant
673 was collected in fresh tube followed by addition of 50% glycerol and 1.5 µL of 1% Coomassie
674 brilliant blue G-250. Samples were loaded in 3-13% gradient gel and subsequently transferred
675 on methanol activated PVDF membrane. Membranes were blocked in 5% skimmed milk for 1
676 hour and incubation was carried out overnight in 4°C under shaking conditions with primary

677 antibodies: MIC10 (Abcam, 84969), MIC13 (custom made by Pineda (Berlin) against human
678 MIC13 peptide CKAREYSKEGWEYVKARTK), MIC19 (Proteintech, 25625-1-AP), MIC25
679 (Proteintech, 20639-1-AP), MIC26 (Thermofisher Scientific, MIC27 (Sigma-Aldrich,
680 HPA000612-100UL), MIC60 (Abcam, ab110329), SLP2 (Abcam, ab102051), MTX1 (Abcam,
681 ab233205). Primary antibodies were washed 3x with TBST and incubated with Goat anti-
682 mouse IgG HRP-conjugated antibody (Abcam, ab97023) or goat anti-rabbit IgG HRP-
683 conjugated antibody (Dianova, 111-035-144) diluted to 1:10000 in 5% skimmed milk in TBST.
684 Chemiluminescent signal was recorded with VILBER LOURMAT Fusion SL (Peqlab) and
685 quantification was performed with ImageJ.

686 **Mitochondria morphology analysis**

687 Flp-In T-REx HEK293 cells were transfected with 1ug of mitochondrially targeted GFP (Mito-
688 GFP) with along with 3.5 µL of GeneJuice. 24 hours post transfection, cells were treated with
689 10 µM cycloheximide and incubated for 2 hours at 37°C in CO_2 incubator. Media was removed
690 following PBS washing three times. Cells were fixed using 4% paraformaldehyde (Sigma-
691 Aldrich, P6148) for 20 mins in room temperature and washed with PBS 3 times. GFP signals
692 were visualized in PerkinElmer spinning disc confocal microscope equipped with a 60× oil
693 objective. Cells were classified as hypertubular, tubular, intermediate or fragmented based on
694 the majority of mitochondrial population present in the particular cell. Cells classified as
695 hypertubular contained large interconnected tubular mitochondrial networks. Cells classified
696 as intermediate contained a comparable ratio of short tubes or fragmented mitochondria, while
697 cells classified as tubular and fragmented contained mostly long tubular and very short
698 mitochondria fragments, respectively.

699 **Stimulated emission depletion (STED) super-resolution nanoscopy**

700 Cells were fixed and permeabilized as described earlier (PLA assay). Permeabilized cells were
701 blocked with 5% goat serum and primary antibody incubation was carried out with 1:100 rabbit
702 anti-MIC60 antibody (custom-made, Pineda (Berlin)), which was generated using the peptide
703 CTDHPEIGEGKPTPALSEEAS against human MIC60, overnight at 4°C and 1:100 Aberrior

704 STAR 635P goat-anti-rabbit (2-0012-007-2) secondary antibody incubated at room
705 temperature for 1 h. STED imaging was performed with the Leica SP8 laser scanning confocal
706 microscope coupled with a STED module. Initially, imaging of 80-nm gold particles (BBI
707 Solutions) was carried out in reflection mode for correct alignment of excitation and depletion
708 laser. A 93x glycerol (N.A = 1.3) objective was used with the pinhole set to 0.6 Airy units and
709 a white light laser excitation wavelength of 633 nm was used for sample excitation. STED
710 depletion was carried out with a pulsed STED depletion laser beam of 775 nm wavelength. A
711 hybrid detector (HyD) was used for signal detection in the range from 643 to 699 nm. 13x
712 magnification was used to acquire images covering a field of view of 9.62 x 9.62 µm. No image
713 processing was performed except smoothing carried out with Fiji software.

714

715 **Electron microscopy**

716 Cells were cultured in petri dishes until about 80% confluency was reached and chemical
717 fixation was carried out using 3% glutaraldehyde buffered with 0.1 M sodium cacodylate, pH
718 7.2, followed by cell scrapping and centrifugation. Cell pellets were washed with 0.1 M sodium
719 cacodylate and embedded in 2% agarose. Cell staining was performed with 1% osmium
720 tetroxide for 50 mins with subsequent incubation in 1% uranyl acetate/1% phosphotungstic
721 acid for 1 hour. Samples were further dehydrated with graded acetone series and embedded
722 in spur epoxy resin for polymerization at 65°C for 24 hours. Ultrathin sections of samples were
723 prepared with microtome and images were captured with transmission electron microscope
724 (Hitachi, H7100) at 75V equipped with Bioscan model 792 camera (Gatan) and analyzed with
725 ImageJ software. The images were randomized and the data was analyzed in a double-blind
726 manner by two scientists. Data analysis was carried out by GraphPad prism. Statistical
727 analysis includes one-way Annova test, outlier test was performed with Grubb's test where
728 indicated using GraphPad Prism.

729

730

731 **Figure Legends**

732 **Figure 1. SLP2 is identified as a novel MIC13 interacting partner. A,** Interactome of MIC13
733 with co-ip (co-immunoprecipitation) coupled mass spectrometry revealed SLP2 as a novel
734 interactor of MIC13. **B,** The interaction between SLP2 and MIC13 was validated by co-ip using
735 FLAG antibody in isolated mitochondria from *MIC13* KO cells stably expressing MIC13-FLAG
736 or empty vector (EV) pMSCVpuro as background control. I: input lanes represent loading of
737 10% of total lysates, E: eluate represent proteins eluted from anti-Flag M2 beads, U: unbound
738 fraction. * non-specific IgG bands. **C,** Co-ip probed for SLP2-MICOS interaction with isolated
739 mitochondria from *SLP2* KO stably expressing pMSCVpuro EV (background control) or SLP2-
740 MYC. Co-ip was performed using MYC-Trap agarose beads. I: Input fraction (10% of total
741 lysate), E: Eluate fraction. YME1L was used as a positive interactor of SLP2 whereas Mt-CO2
742 and HSP60 served as non-interactors. All the MICOS subunits were present in the elution
743 fraction from SLP2-MYC co-ip. **D,** Proximity ligation assay (PLA) in HeLa cells with antibodies
744 against MICOS subunits and SLP2. PLA signals are shown as red spots indicating respective
745 protein interactions. SLP2 alone and Mt-CO2 & SLP2 antibodies were probed as negative
746 controls.

747 **Figure 2. SLP2 forms an interaction hub with MICOS complex proteins. A,** Co-ip-western
748 blot analysis from *SLP2* KO or MIC10-subcomplex KO (left) and **B**, *SLP2* KO or MIC60-
749 subcomplex KO (right) stably expressing pMSCVpuro EV or SLP2-MYC showed that SLP2
750 can stably interact with any remaining MICOS subunits even upon the loss of individual MICOS
751 subunits. Due to low abundance of MICOS proteins in *MIC60* KO cells, overexposed blots
752 were represented showing independent interaction of MIC13, MIC26, MIC27 and MIC19 with
753 SLP2 in absence of MIC60. I: Input fraction (10% of total lysate), E: Eluate fraction. **C,** BN-
754 PAGE with isolated mitochondria from WT cells revealed a co-migration pattern of SLP2 with
755 higher molecular weight MICOS complex. **D,** Scaffolding model depicting interaction of SLP2
756 as an auxiliary MICOS subunits shows that SLP2 provides a scaffold for interaction of MICOS
757 subunits.

758 **Figure 3. Loss of SLP2 leads to aberrant cristae structure and reduced MIC26 levels. A,**
759 Steady state levels of MICOS proteins with western blot analysis from WT, *SLP2* KO and *SLP2*
760 KO cells stably expressing pMSCVpuro EV or SLP2-MYC. **B,** BN-PAGE of isolated
761 mitochondria from WT and *SLP2* KO cells stained for MICOS subunits. **C,** Western blot
762 analysis of steady state levels of MICOS proteins from WT and *SLP2* KO cells stably
763 expressing pGIPZ-control shRNA or YME1L shRNA (knockdown represented as KD). **D,** A
764 model depicting the role of SLP2 in stabilizing MIC26 by regulating YME1L-mediated
765 proteolysis. **E,** TEM images from WT, *SLP2* KO and *MIC26* KO cells. *SLP2* KO shows
766 accumulation of swollen cristae, while *MIC26* KO shows interconnected cristae arranged in a
767 honeycomb manner. **F,** Cristae number and CJs per mitochondrial section quantified from
768 TEM images. Statistical analysis was performed with one-way ANOVA. *P-value ≤ 0.05, **P-
769 value ≤ 0.01, ***P-value ≤ 0.001.

770 **Figure 4. SLP2 and MIC13 synergistically regulate assembly of MIC60-subcomplex. A,**
771 Assessment of steady state levels of MICOS proteins with western blot from WT, *MIC13* KO,
772 *SLP2* KO and *MIC13-SLP2* DKO cells. **B,** BN-PAGE of isolated mitochondria from WT, *MIC13*
773 KO, *SLP2* KO and *MIC13-SLP2* DKO cells to assess MICOS assembly. *MIC13-SLP2* DKO
774 showed reduced MIC60 assembly in MICOS complex compared to any single KO. **C,** A model
775 depicting that MIC60-subcomplex assembly is dependent on SLP2-MIC13 axis. **D**, TEM
776 images displaying mitochondrial morphology from WT, *MIC13* KO, *SLP2* KO and *MIC13-SLP2*
777 DKO cells. **E,** Quantification of number of cristae and CJs per mitochondrial section obtained
778 from TEM. *P-value ≤ 0.05, **P-value ≤ 0.01, ***P-value ≤ 0.001.

779 **Figure 5. SLP2 specifically regulates assembly kinetics of MIC60. A,** WT cells stably
780 expressing pLIX403 EV and *MIC13* KO, *MIC13-SLP2* DKO cells stably expressing pLIX403-
781 MIC13-FLAG were treated with 1 µg/ml of doxycycline (Dox) for indicated time points and
782 western blot analysis depicting steady state levels of MICOS proteins upon induction of MIC13-
783 FLAG are shown. **B,** BN-PAGE with isolated mitochondria from WT cells stably expressing
784 pLIX403 EV, and *MIC13* KO and *MIC13-SLP2 DKO* cells stably expressing pLIX403-MIC13-

785 FLAG treated with 1 µg/ml of doxycycline (Dox) for indicated time points showing stable
786 incorporation of MIC13-FLAG in MICOS complex. **C,** Blue native PAGE with isolated
787 mitochondria from WT cells stably expressing pLIX403 EV, and *MIC13* KO and *MIC13-SLP2*
788 *DKO* cells stably expressing pLIX403-MIC13-FLAG treated with 1 µg/ml of Dox for indicated
789 time points was probed for MIC10, MIC27 and MIC60 antibody. It shows that kinetics of MIC60
790 assembly was dependent on SLP2. **D,** A model depicting the assembly kinetics of MIC60 in
791 MICOS complex depends on SLP2.

792 **Figure 6. MIC13-YME1L and SLP2-YME1L axes stabilize MIC10- and MIC60-subcomplex**
793 **assembly in a co-dependent manner. A,** WT, *MIC13* KO, *SLP2* KO, *MIC13-SLP2* DKO
794 stably expressing pGIPZ-Control shRNA or pGIPZ-YME1L shRNA (knockdown represented
795 as KD) subjected to western blot to assess steady state levels of MICOS proteins. The levels
796 of MIC10, MIC26 and MIC27 were dependent on YME1L-mediated proteolysis. **B,** BN-PAGE
797 with isolated mitochondria from WT, *MIC13* KO, *SLP2* KO, *MIC13-SLP2 DKO* stably
798 expressing pGIPZ-Control shRNA or pGIPZ- YME1L shRNA. Red arrow indicates downshift
799 of MIC60 and green arrow indicates upshift of MIC60 in BN-PAGE. **C,** Mitochondrial cristae
800 morphology accessed using TEM from WT, *MIC13* KO, *SLP2* KO, *MIC13-SLP2* DKO stably
801 expressing pGIPZ-Control shRNA or pGIPZ-YME1L shRNA. Scale bar represents 0.5 µm. Red
802 arrows depict CJs in the mitochondrial section showing a partial beneficial effect on cristae
803 morphology upon YME1L depletion. **D,** Quantification of crista and CJs per mitochondrial
804 section. Outliers were removed with Grubbs' method and statistical significance was analysed
805 by one-way ANOVA. *P-value ≤ 0.05, **P-value ≤ 0.01, ***P-value ≤ 0.001.

806 **Figure 7. MIC13-SLP2 axis is required for formation of MIC60 punctae**. **A,** STED
807 nanoscopy images from WT, *MIC13* KO, *SLP2* KO and *MIC13-SLP2 DKO* cells displaying
808 MIC60 punctae. White arrows indicate individual MIC60 punctae in a rail-like arrangement in
809 WT cells. Arrow heads depict perturbed MIC60 punctae in *MIC13* KO and *SLP2* KO. Yellow
810 arrow with curve depicts dispersed MIC60 punctae in *MIC13-SLP2* DKO cells. **B,** A
811 comprehensive schematic model of CJ formation illustrating the novel quality control process

812 orchestrated by the MIC13-YME1L and SLP2-YME1L axis, which facilitates the formation of
813 the SLP2-MIC10-subcomplex, known as the "seeder complex." The seeder complex promotes
814 the 'seeding' or assembly of the MIC60-subcomplex and the essential MIB protein MTX1,
815 consequently playing a crucial role in defining the formation of MIC60 puncta and the MICOS-
816 MIB complex. This mechanistically promote the formation of CJ and contact between IM and
817 OM.

818 **Supplementary**

819 **Supplementary Figure 1.** A heatmap and graph represent the normalized occurrence of SLP2
820 and MICOS subunits in complexome profiling data obtained from the HEK293 cells studied
821 previously (Anand et al., 2016). SLP2 co-clustered with high molecular weight MICOS complex
822 around 2000 kDa.

823 **Supplementary Figure 2. SLP2 promotes stress induced mitochondrial hyperfusion**
824 **independent of MICOS**. A, Assessment of mitochondrial morphologies from WT, MIC13 KO,
825 SLP2 KO and MIC13-SLP2 DKO cells post treatment with 10 μM cycloheximide for 2 hours.
826 B, Percentage of cells displaying tubular, intermediate, fragmented or hyperfused mitochondria
827 (n= 3). *P-value ≤ 0.05, **P-value ≤ 0.01, ***P-value ≤ 0.001. Data represented as mean with
828 standard error of mean. Scale bar represented as 15 μm.

829 **Supplementary Figure 3.** Co-ip of MIC13-Flag using anti -Flag M2 beads with isolated
830 mitochondria from *MIC13* KO stably expressing pMSCVpuro EV (negative control) and
831 MIC13-Flag expressing in *MIC13* KO and *MIC13-SLP2* DKO cells. The interaction of
832 MIC13 with other MICOS subunits was unaffected upon loss of SLP2. YME1L was
833 found as a novel interactor of MIC13. MIC13 -YME1L interaction is independent of SLP2.

834 **Supplementary Figure 4. SLP2 specifically regulates assembly kinetics of MIC60. A,**
835 WT cells stably expressing pLIX403 EV and *MIC13* KO, *MIC13-SLP2* DKO cells stably

836 expressing pLIX403-MIC13-FLAG were treated with 1 µg/ml of doxycycline (Dox) for indicated
837 time points. **B,** Blue native PAGE with isolated mitochondria from WT cells stably expressing
838 pLIX403 EV, and *MIC13* KO and *MIC13-SLP2 DKO* cells stably expressing pLIX403-MIC13-
839 FLAG treated with 1 µg/ml of Dox for indicated time points was probed for MIC60 antibody. It
840 shows that kinetics of MIC60 assembly was dependent on SLP2.

841 **Supplementary Table 1. Interactome of MIC13**

842 **Supplementary Table 2. List of cell lines prepared**

843 **Supplementary Table 3. Primers sequence for cloning**

844 **AUTHOR CONTRIBUTIONS**

845 Ritam Naha: Investigation, methodology, data curation, formal analysis, visualization, writing—
846 original draft, writing—review and editing.

847 Rebecca Strohm: Investigation, methodology, data curation, formal analysis.

848 Jennifer Urbach: Investigation, methodology, formal analysis.

849 Ilka Wittig: investigation, methodology, formal analysis, data curation.

850 Arun Kumar Kondadi: formal analysis, supervision, validation, funding acquisition, writing—
851 review and editing.

852 Andreas S. Reichert: supervision, funding acquisition, writing—review and editing.

853 Ruchika Anand: conceptualization, data curation, formal analysis, supervision, methodology,
854 funding acquisition, project administration, writing—original draft, writing—review and editing.

855 **Acknowledgements**

856 Authors would like to thank Andrea Borchardt, Tanja Portugall for their technical assistance in
857 cloning and electron microscopy. We further thank Anny Garces Palacio as student assistant
858 for performing microscopy experiments. Electron microscopy was performed at the Core

facility for electron microscopy (CFEM) at the medical faculty of the Heinrich Heine University Düsseldorf. The STED imaging experiments were performed at the Centre for Advanced Imaging (CAi) at Heinrich Heine University Düsseldorf.

The research was supported by funding from Medical faculty of Heinrich Heine University Düsseldorf, Foko-02/2015 (RA & ASR), FoKo-2020-71 (RA), FoKo 2022-11 (AKK) and Deutsche Forschungsgemeinschaft (DFG) grant, AN 1440/3-1 (RA), AN 1440/4-1 (RA), KO 6519/1-1 (AKK) and SFB 1208 project B12 (ID 267205415) to ASR.

Declaration of interests

The authors declare no competing interests.

References

An J, Shi J, He Q, Lui K, Liu Y, Huang Y, Sheikh MS (2012) CHCM1/CHCHD6, novel mitochondrial protein linked to regulation of mitofilin and mitochondrial cristae morphology. *The Journal of biological chemistry* 287: 7411-26

Anand R, Kondadi AK, Meisterknecht J, Golombek M, Nortmann O, Riedel J, Peifer-Weiss L, Brocke-Ahmadinejad N, Schlutermann D, Stork B, Eichmann TO, Wittig I, Reichert AS (2020) MIC26 and MIC27 cooperate to regulate cardiolipin levels and the landscape of OXPHOS complexes. *Life Sci Alliance* 3

Anand R, Reichert AS, Kondadi AK (2021) Emerging Roles of the MICOS Complex in Cristae Dynamics and Biogenesis. *Biology (Basel)* 10

Anand R, Strecker V, Urbach J, Wittig I, Reichert AS (2016) Mic13 Is Essential for Formation of Crista Junctions in Mammalian Cells. *PloS one* 11: e0160258

Barbot M, Jans DC, Schulz C, Denkert N, Kroppen B, Hoppert M, Jakobs S, Meinecke M (2015) Mic10 oligomerizes to bend mitochondrial inner membranes at cristae junctions. *Cell metabolism* 21: 756-63

Beninca C, Zanette V, Brischigliaro M, Johnson M, Reyes A, Valle DAD, A JR, Degiorgi A, Yeates A, Telles BA, Prudent J, Baruffini E, ML SFS, RL RdS, Fernandez-Vizarra E, A JW, Zeviani M (2021a) Mutation in the MICOS subunit gene APOO (MIC26) associated with an X-

886 linked recessive mitochondrial myopathy, lactic acidosis, cognitive impairment and autistic
887 features. *J Med Genet* 58: 155-167
888 Beninca C, Zanette V, Brischigliaro M, Johnson M, Reyes A, Valle DAD, A JR, Degiorgi A,
889 Yeates A, Telles BA, Prudent J, Baruffini E, ML SFS, RL RdS, Fernandez-Vizarra E, Whitworth
890 AJ, Zeviani M (2021b) Mutation in the MICOS subunit gene APOO (MIC26) associated with
891 an X-linked recessive mitochondrial myopathy, lactic acidosis, cognitive impairment and
892 autistic features. *J Med Genet* 58: 155-167
893 Bock-Bierbaum T, Funck K, Wollweber F, Lisicki E, von der Malsburg K, von der Malsburg A,
894 Laborenz J, Noel JK, Hessenberger M, Jungbluth S, Bernert C, Kunz S, Riedel D, Lilie H,
895 Jakobs S, van der Laan M, Daumke O (2022) Structural insights into crista junction formation
896 by the Mic60-Mic19 complex. *Science advances* 8: eabo4946
897 Bohnert M, Zerbes RM, Davies KM, Muhleip AW, Rampelt H, Horvath SE, Boenke T, Kram A,
898 Perschil I, Veenhuis M, Kuhlbrandt W, van der Klei IJ, Pfanner N, van der Laan M (2015)
899 Central role of Mic10 in the mitochondrial contact site and cristae organizing system. *Cell*
900 *metabolism* 21: 747-55
901 Chiu J, Tillett D, Dawes IW, March PE (2008) Site-directed, Ligase-Independent Mutagenesis
902 (SLIM) for highly efficient mutagenesis of plasmids greater than 8kb. *Journal of microbiological*
903 *methods* 73: 195-8
904 Christie DA, Lemke CD, Elias IM, Chau LA, Kirchhof MG, Li B, Ball EH, Dunn SD, Hatch GM,
905 Madrenas J (2011) Stomatin-like protein 2 binds cardiolipin and regulates mitochondrial
906 biogenesis and function. *Molecular and cellular biology* 31: 3845-56
907 Godiker J, Gruneberg M, DuChesne I, Reunert J, Rust S, Westermann C, Wada Y, Classen
908 G, Langhans CD, Schlingmann KP, Rodenburg RJ, Pohlmann R, Marquardt T (2018) QIL1-
909 dependent assembly of MICOS complex-lethal mutation in C19ORF70 resulting in liver
910 disease and severe neurological retardation. *Journal of human genetics* 63: 707-716
911 Guarani V, Jardel C, Chretien D, Lombes A, Benit P, Labasse C, Lacene E, Bourillon A, Imbard
912 A, Benoist JF, Dorboz I, Gilleron M, Goetzman ES, Gaignard P, Slama A, Elmaleh-Berges M,

913 Romero NB, Rustin P, Ogier de Baulny H, Paulo JA et al. (2016) QIL1 mutation causes MICOS
914 disassembly and early onset fatal mitochondrial encephalopathy with liver disease. *eLife* 5
915 Guarani V, McNeill EM, Paulo JA, Huttlin EL, Frohlich F, Gygi SP, Van Vactor D, Harper JW
916 (2015) QIL1 is a novel mitochondrial protein required for MICOS complex stability and cristae
917 morphology. *eLife* 4
918 Hessenberger M, Zerbes RM, Rampelt H, Kunz S, Xavier AH, Purfurst B, Lilie H, Pfanner N,
919 van der Laan M, Daumke O (2017) Regulated membrane remodeling by Mic60 controls
920 formation of mitochondrial crista junctions. *Nature communications* 8: 15258
921 Huynen MA, Muhlmeister M, Gotthardt K, Guerrero-Castillo S, Brandt U (2016) Evolution and
922 structural organization of the mitochondrial contact site (MICOS) complex and the
923 mitochondrial intermembrane space bridging (MIB) complex. *Biochimica et biophysica acta*
924 1863: 91-101
925 Jans DC, Wurm CA, Riedel D, Wenzel D, Stagge F, Deckers M, Rehling P, Jakobs S (2013)
926 STED super-resolution microscopy reveals an array of MINOS clusters along human
927 mitochondria. *Proceedings of the National Academy of Sciences of the United States of*
928 *America* 110: 8936-41
929 Kondadi AK, Anand R, Hansch S, Urbach J, Zobel T, Wolf DM, Segawa M, Liesa M, Shirihai
930 OS, Weidtkamp-Peters S, Reichert AS (2020) Cristae undergo continuous cycles of membrane
931 remodelling in a MICOS-dependent manner. *EMBO reports* 21: e49776
932 Kulak NA, Pichler G, Paron I, Nagaraj N, Mann M (2014) Minimal, encapsulated proteomic-
933 sample processing applied to copy-number estimation in eukaryotic cells. *Nat Methods* 11:
934 319-24
935 Li H, Ruan Y, Zhang K, Jian F, Hu C, Miao L, Gong L, Sun L, Zhang X, Chen S, Chen H, Liu
936 D, Song Z (2016) Mic60/Mitofilin determines MICOS assembly essential for mitochondrial
937 dynamics and mtDNA nucleoid organization. *Cell death and differentiation* 23: 380-92
938 Mannella CA, Lederer WJ, Jafri MS (2013) The connection between inner membrane topology
939 and mitochondrial function. *Journal of molecular and cellular cardiology* 62: 51-7

940 Monzel AS, Enríquez JA, Picard M (2023) Multifaceted mitochondria: moving mitochondrial
941 science beyond function and dysfunction. *Nat Metab* 5: 546-562
942 Mukherjee I, Ghosh M, Meinecke M (2021) MICOS and the mitochondrial inner membrane
943 morphology - when things get out of shape. *FEBS letters* 595: 1159-1183
944 Olsen VJ, Godoy DMFL, Li G, Macek B, Mortensen P, Pesch R, Makarov A, Lange O, Horning
945 S, Mann M (2005) Parts per Million Mass Accuracy on an Orbitrap Mass Spectrometer via
946 Lock Mass Injection into a C-trap. *Molecular & Cellular Proteomics* 4: 2010-2021
947 Ott C, Dorsch E, Fraunholz M, Straub S, Kozjak-Pavlovic V (2015) Detailed analysis of the
948 human mitochondrial contact site complex indicate a hierarchy of subunits. *PloS one* 10:
949 e0120213
950 Peifer-Weiß L, Kurban M, David C, Lubeck M, Kondadi AK, Nemer G, Reichert AS, Anand R
951 (2023) A X-linked nonsense APOO/MIC26 variant causes a lethal mitochondrial disease with
952 progeria-like phenotypes. *Clinical genetics*
953 Perkins G, Renken C, Martone ME, Young SJ, Ellisman M, Frey T (1997) Electron tomography
954 of neuronal mitochondria: three-dimensional structure and organization of cristae and
955 membrane contacts. *Journal of structural biology* 119: 260-72
956 Russell BE, Whaley KG, Bove KE, Labilloy A, Lombardo RC, Hopkin RJ, Leslie ND, Prada C,
957 Assouline Z, Barcia G, Bouchereau J, Chomton M, Debray D, Dorboz I, Durand P, Gaignard
958 P, Habes D, Jardel C, Labarthe F, Levy J et al. (2019) Expanding and Underscoring the
959 Hepato-Encephalopathic Phenotype of QIL1/MIC13. *Hepatology* 70: 1066-1070
960 Sakowska P, Jans DC, Mohanraj K, Riedel D, Jakobs S, Chacinska A (2015) The Oxidation
961 Status of Mic19 Regulates MICOS Assembly. *Molecular and cellular biology* 35: 4222-37
962 Scorrano L, Ashiya M, Buttle K, Weiler S, Oakes SA, Mannella CA, Korsmeyer SJ (2002) A
963 distinct pathway remodels mitochondrial cristae and mobilizes cytochrome c during apoptosis.
964 *Developmental cell* 2: 55-67
965 Stenton SL, Prokisch H (2020) Genetics of mitochondrial diseases: Identifying mutations to
966 help diagnosis. *EBioMedicine* 56: 102784

967 Stephan T, Brüser C, Deckers M, Steyer AM, Balzarotti F, Barbot M, Behr TS, Heim G, Hübner
968 W, Ilgen P, Lange F, Pacheu-Grau D, Pape JK, Stoldt S, Huser T, Hell SW, Möbius W, Rehling
969 P, Riedel D, Jakobs S (2020) MICOS assembly controls mitochondrial inner membrane
970 remodeling and crista junction redistribution to mediate cristae formation. *The EMBO journal*
971 39: e104105
972 Stoldt S, Stephan T, Jans DC, Bruser C, Lange F, Keller-Findeisen J, Riedel D, Hell SW,
973 Jakobs S (2019) Mic60 exhibits a coordinated clustered distribution along and across yeast
974 and mammalian mitochondria. *Proceedings of the National Academy of Sciences of the United*
975 *States of America* 116: 9853-9858
976 Tang J, Zhang K, Dong J, Yan C, Hu C, Ji H, Chen L, Chen S, Zhao H, Song Z (2020) Sam50-
977 Mic19-Mic60 axis determines mitochondrial cristae architecture by mediating mitochondrial
978 outer and inner membrane contact. *Cell death and differentiation* 27: 146-160
979 Tarasenko D, Barbot M, Jans DC, Kroppen B, Sadowski B, Heim G, Mobius W, Jakobs S,
980 Meinecke M (2017) The MICOS component Mic60 displays a conserved membrane-bending
981 activity that is necessary for normal cristae morphology. *The Journal of cell biology* 216: 889-
982 899
983 Tondera D, Grandemange S, Jourdain A, Karbowski M, Mattenberger Y, Herzig S, Da Cruz S,
984 Clerc P, Raschke I, Merkwirth C, Ehses S, Krause F, Chan DC, Alexander C, Bauer C, Youle
985 R, Langer T, Martinou JC (2009) SLP-2 is required for stress-induced mitochondrial
986 hyperfusion. *The EMBO journal* 28: 1589-600
987 Tsai PI, Lin CH, Hsieh CH, Papakyrikos AM, Kim MJ, Napolioni V, Schoor C, Couthouis J, Wu
988 RM, Wszolek ZK, Winter D, Greicius MD, Ross OA, Wang X (2018) PINK1 Phosphorylates
989 MIC60/Mitofilin to Control Structural Plasticity of Mitochondrial Crista Junctions. *Molecular cell*
990 69: 744-756 e6
991 Urbach J, Kondadi AK, David C, Naha R, Deinert K, Reichert AS, Anand R (2021) Conserved
992 GxxxG and WN motifs of MIC13 are essential for bridging two MICOS subcomplexes.
993 *Biochimica et biophysica acta Biomembranes* 1863: 183683

994 Viana MP, Levytskyy RM, Anand R, Reichert AS, Khalimonchuk O (2021) Protease OMA1
995 modulates mitochondrial bioenergetics and ultrastructure through dynamic association with
996 MICOS complex. *iScience* 24: 102119
997 Wai T, Saita S, Nolte H, Muller S, Konig T, Richter-Dennerlein R, Sprenger HG, Madrenas J,
998 Muhlmeister M, Brandt U, Kruger M, Langer T (2016) The membrane scaffold SLP2 anchors
999 a proteolytic hub in mitochondria containing PARL and the i-AAA protease YME1L. *EMBO*
1000 *reports* 17: 1844-1856
1001 Weber TA, Koob S, Heide H, Wittig I, Head B, van der Bliek A, Brandt U, Mittelbronn M,
1002 Reichert AS (2013) APOOL is a cardiolipin-binding constituent of the Mitofilin/MINOS protein
1003 complex determining cristae morphology in mammalian mitochondria. *PloS one* 8: e63683
1004 Xie J, Marusich MF, Souda P, Whitelegge J, Capaldi RA (2007) The mitochondrial inner
1005 membrane protein mitofilin exists as a complex with SAM50, metaxins 1 and 2, coiled-coil-
1006 helix coiled-coil-helix domain-containing protein 3 and 6 and DnaJC11. *FEBS letters* 581:
1007 3545-9
1008 Zeharia A, Friedman JR, Tobar A, Saada A, Konen O, Fellig Y, Shaag A, Nunnari J, Elpeleg
1009 O (2016) Mitochondrial hepato-encephalopathy due to deficiency of QIL1/MIC13 (C19orf70),
1010 a MICOS complex subunit. *European journal of human genetics : EJHG* 24: 1778-1782
1011 Zerbes RM, Hoss P, Pfanner N, van der Laan M, Bohnert M (2016) Distinct Roles of Mic12
1012 and Mic27 in the Mitochondrial Contact Site and Cristae Organizing System. *Journal of*
1013 *molecular biology* 428: 1485-92
1014 Zerbes RM, van der Klei IJ, Veenhuis M, Pfanner N, van der Laan M, Bohnert M (2012) Mitofilin
1015 complexes: conserved organizers of mitochondrial membrane architecture. *Biological*
1016 *chemistry* 393: 1247-61

1017

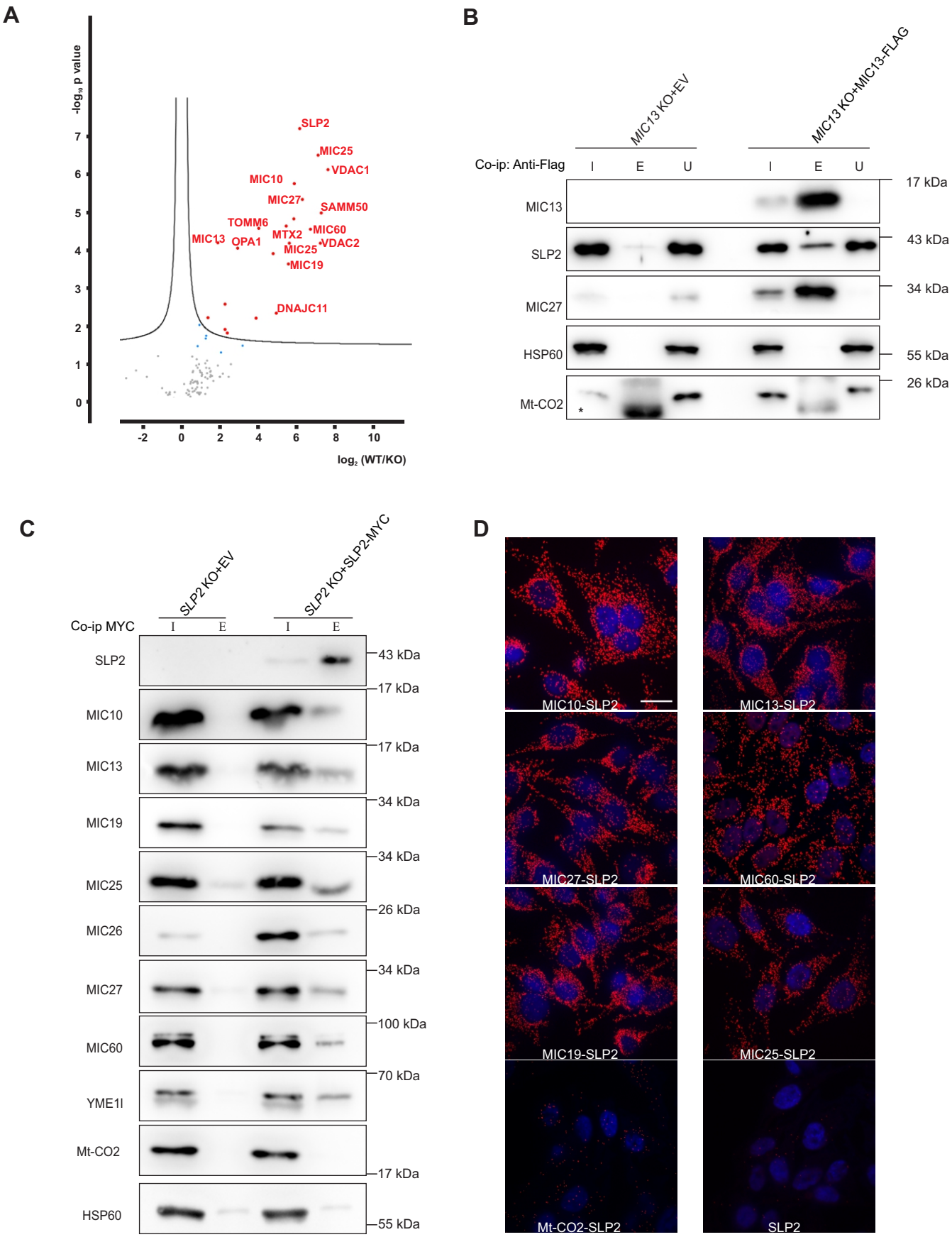

Figure 1. SLP2 is identified as a novel MIC13 interacting partner

Figure 1. SLP2 is identified as a novel MIC13 interacting partner. A, Interactome of MIC13 with co-ip (co-immunoprecipitation) coupled mass spectrometry revealed SLP2 as a novel interactor of MIC13. **B,** The interaction between SLP2 and MIC13 was validated by co-ip using FLAG antibody in isolated mitochondria from *MIC13* KO cells stably expressing MIC13-FLAG or empty vector (EV) pMSCVpuro as background control. I: input lanes represent loading of 10% of total lysates, E: eluate represent proteins eluted from anti-Flag M2 beads, U: unbound fraction. * non-specific IgG bands. **C,** Co-ip probed for SLP2-MICOS interaction with isolated mitochondria from *SLP2* KO stably expressing pMSCVpuro EV (background control) or SLP2-MYC. Co-ip was performed using MYC-Trap agarose beads. I: Input fraction (10% of total lysate), E: Eluate fraction. YME1L was used as a positive interactor of SLP2 whereas Mt-CO2 and HSP60 served as non-interactors. All the MICOS subunits were present in the elution fraction from SLP2-MYC co-ip. **D,** Proximity ligation assay in HeLa cells with antibodies against MICOS subunits and SLP2. PLA signals are shown as red spots indicating respective protein interactions. SLP2 alone and Mt-CO2 & SLP2 antibodies were probed as negative controls.

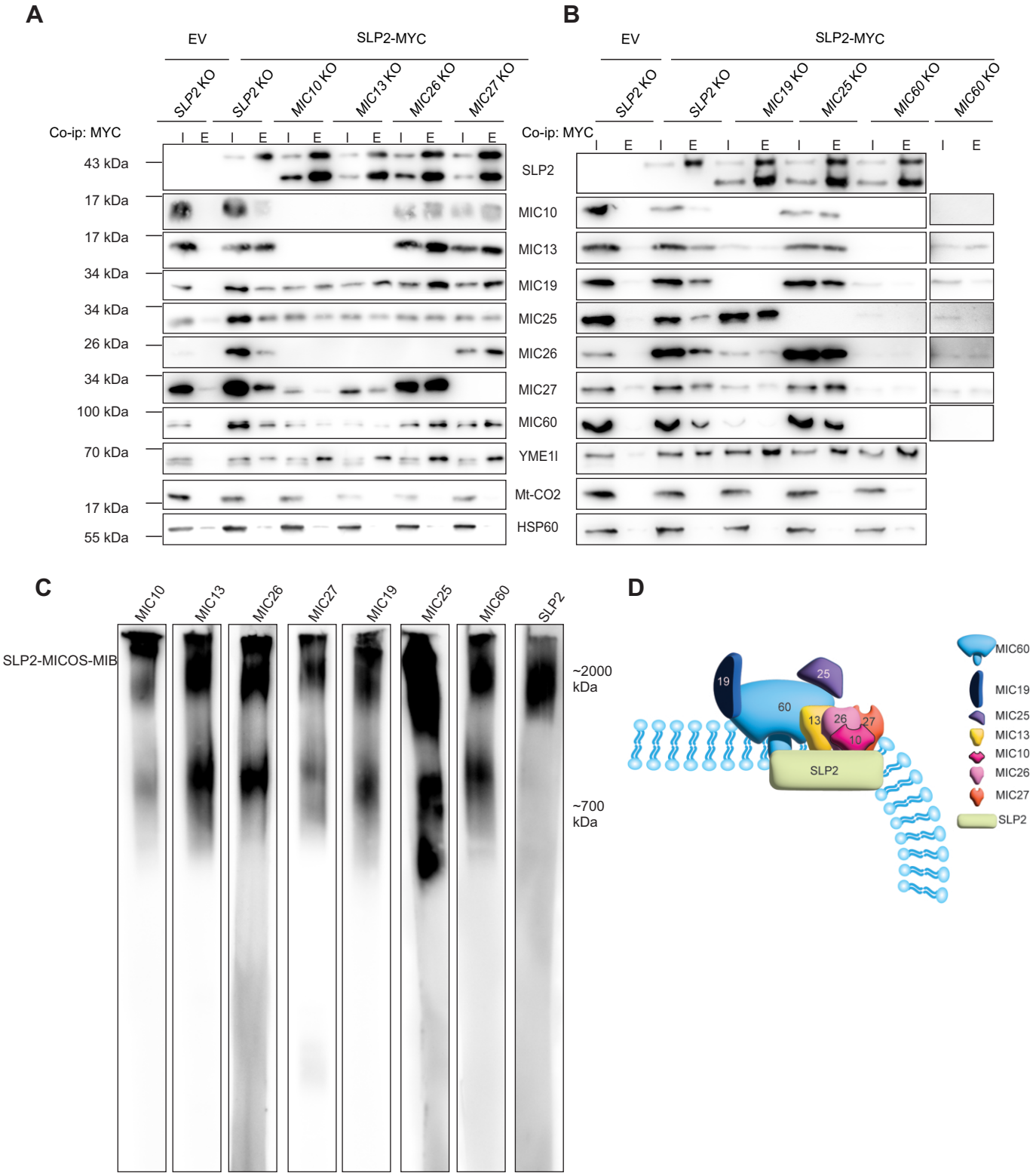

Figure 2. SLP2 forms an interaction hub with MICOS complex proteins

Figure 2. SLP2 forms an interaction hub with MICOS complex proteins. A, Co-ip-western blot analysis from *SLP2* KO or MIC10-subcomplex KO (left) and **B**, *SLP2* KO or MIC60-subcomplex KO (right) stably expressing pMSCVpuro EV or SLP2-MYC showed that SLP2 can stably interact with any remaining MICOS subunits even upon the loss of individual MICOS subunits. Due to low abundance of MICOS proteins in *MIC60* KO cells, overexposed blots were represented showing independent interaction of MIC13, MIC26, MIC27 and MIC19 with SLP2 in absence of MIC60. I: Input fraction (10% of total lysate), E: Eluate fraction. **C,** BN-PAGE with isolated mitochondria from WT cells revealed a co-migration pattern of SLP2 with higher molecular weight MICOS complex. **D,** Scaffolding model depicting interaction of SLP2 with MICOS subunits shows that SLP2 provides a scaffold for interaction of MICOS subunits.

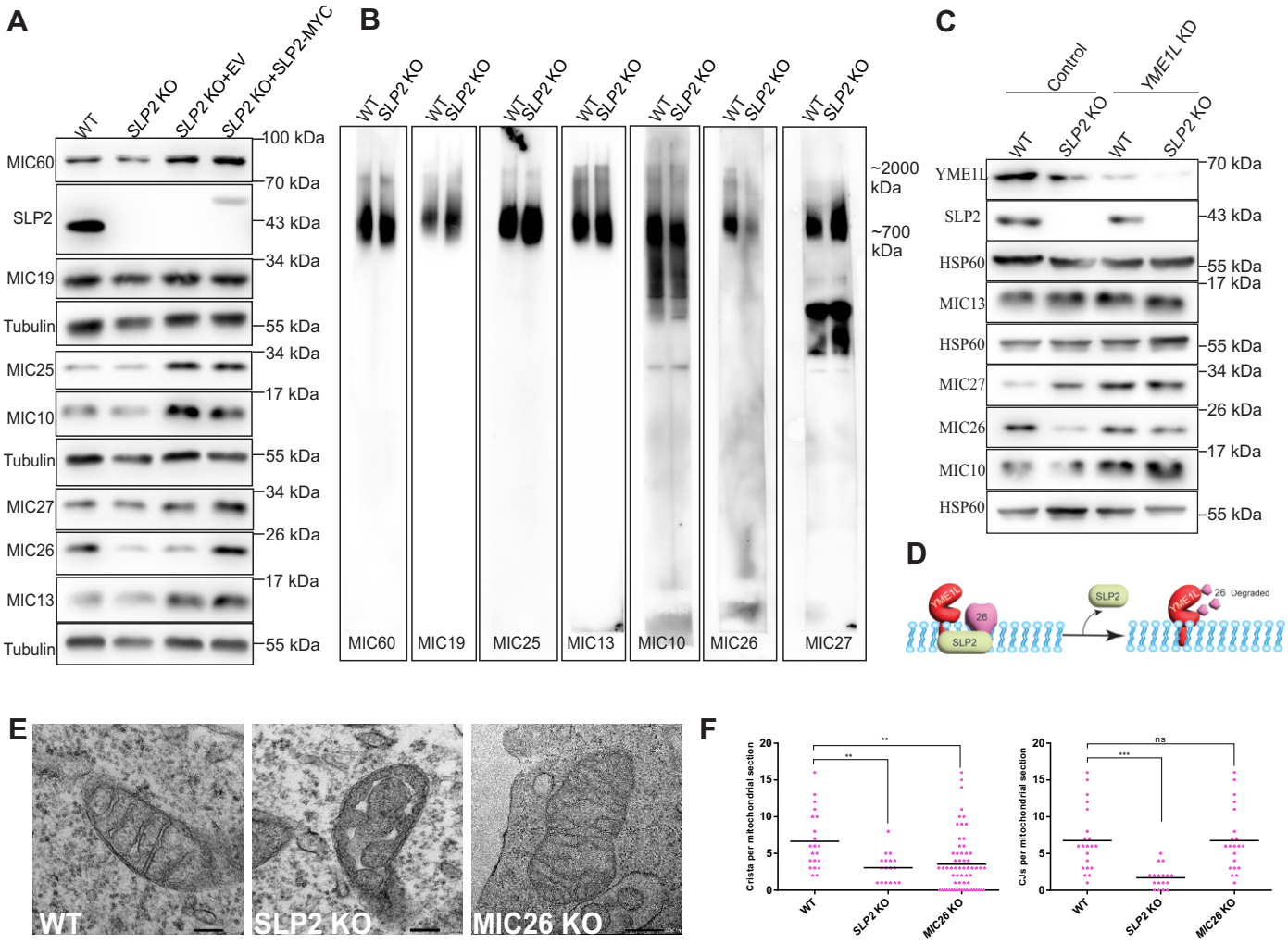

Figure 3. Loss of SLP2 leads to aberrant cristae structure and reduced MIC26 levels

Figure 3. Figure 3. Loss of SLP2 leads to aberrant cristae structure and reduced MIC26 levels. A, Steady state levels of MICOS proteins with western blot analysis from WT, *SLP2* KO and *SLP2* KO cells stably expressing pMSCVpuro EV or SLP2-MYC. **B,** BN-PAGE of isolated mitochondria from WT and *SLP2* KO cells stained for MICOS subunits. **C,** Western blot analysis of steady state levels of MICOS proteins from WT and *SLP2* KO cells stably expressing pGIPZ-control shRNA or YME1L shRNA (knockdown represented as KD). **D,** A model depicting the role of SLP2 in stabilizing MIC26 by regulating YME1L-mediated proteolysis. **E,** TEM images from WT, *SLP2* KO and *MIC26* KO cells. *SLP2* KO shows accumulation of swollen cristae, while *MIC26* KO shows interconnected cristae arranged in a honeycomb manner. **F,** Cristae number and CJs per mitochondrial section quantified from TEM images. Statistical analysis was performed with one-way ANOVA. *P-value $\leq$ 0.05, **P-value $\leq$ 0.01, ***P-value $\leq$ 0.001.

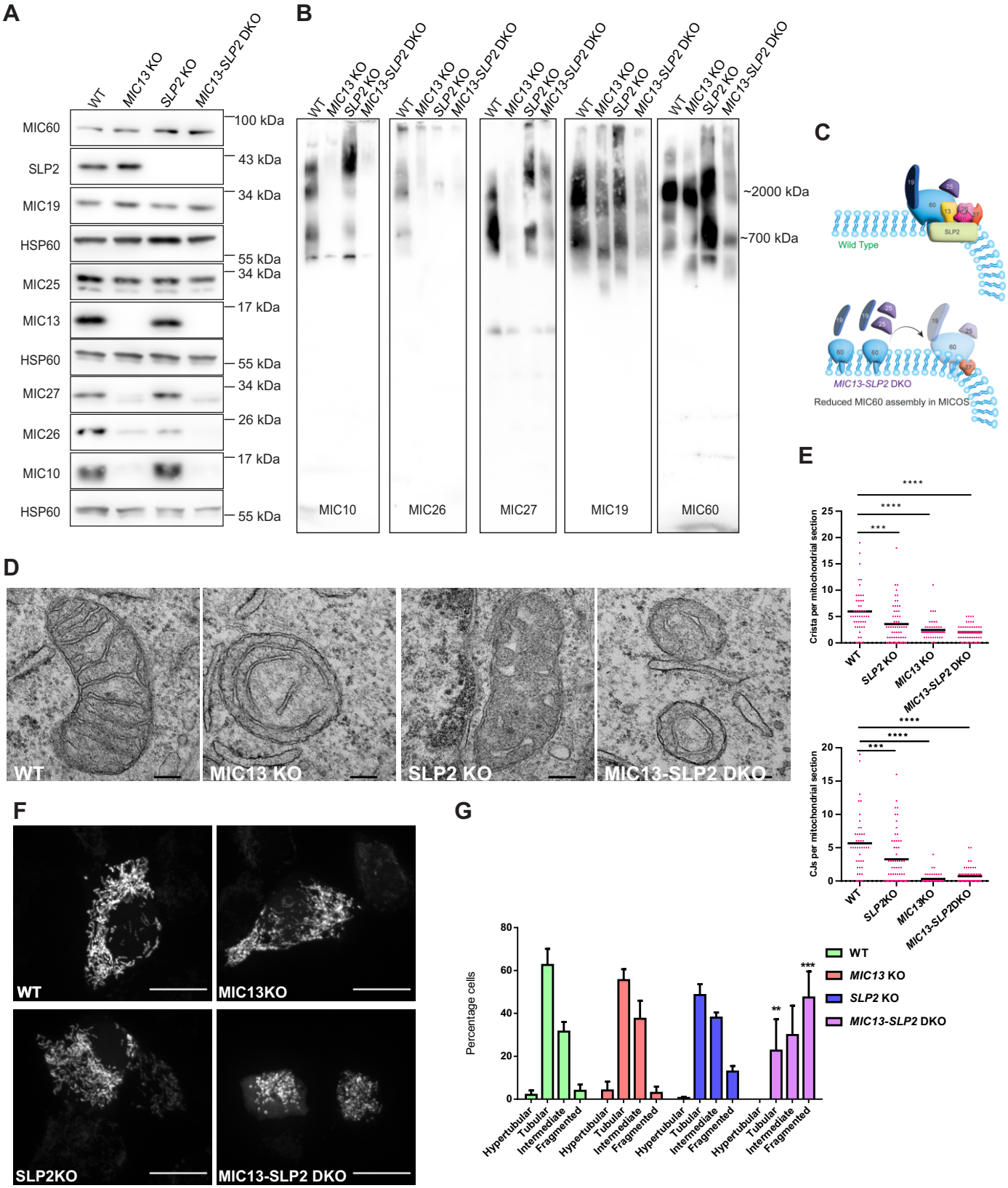

Figure 4. SLP2 and MIC13 regulate assembly of MIC60-subcomplex

Figure 4. SLP2 and MIC13 synergistically regulate assembly of MIC60-subcomplex. **A,** Assessment of steady state levels of MICOS proteins with western blot from WT, *MIC13* KO, *SLP2* KO and *MIC13-SLP2* DKO cells. **B,** BN-PAGE of isolated mitochondria from WT, *MIC13* KO, *SLP2* KO and *MIC13-SLP2* DKO cells to assess MICOS assembly. *MIC13-SLP2* DKO showed reduced MIC60 assembly in MICOS complex compared to any single KO. **C,** A model depicting that MIC60-subcomplex assembly is dependent on SLP2-MIC13 axis. **D**, TEM images displaying mitochondrial morphology from WT, *MIC13* KO, *SLP2* KO and *MIC13-SLP2* DKO cells. **E,** Quantification of number of cristae and CJs per mitochondrial section obtained from TEM. *P-value ≤ 0.05, **P-value ≤ 0.01, ***P-value ≤ 0.001.**F**, Assessment of mitochondrial morphologies from WT, *MIC13* KO, *SLP2* KO and *MIC13-SLP2* DKO cells. **G**, Percentage of cells displaying tubular, intermediate, fragmented or hyperfused mitochondria (n= 3). *P-value ≤ 0.05, **P-value ≤ 0.01, ***P-value ≤ 0.001. Data represented as mean with standard error of mean. Scale bar represented as 15 µm.

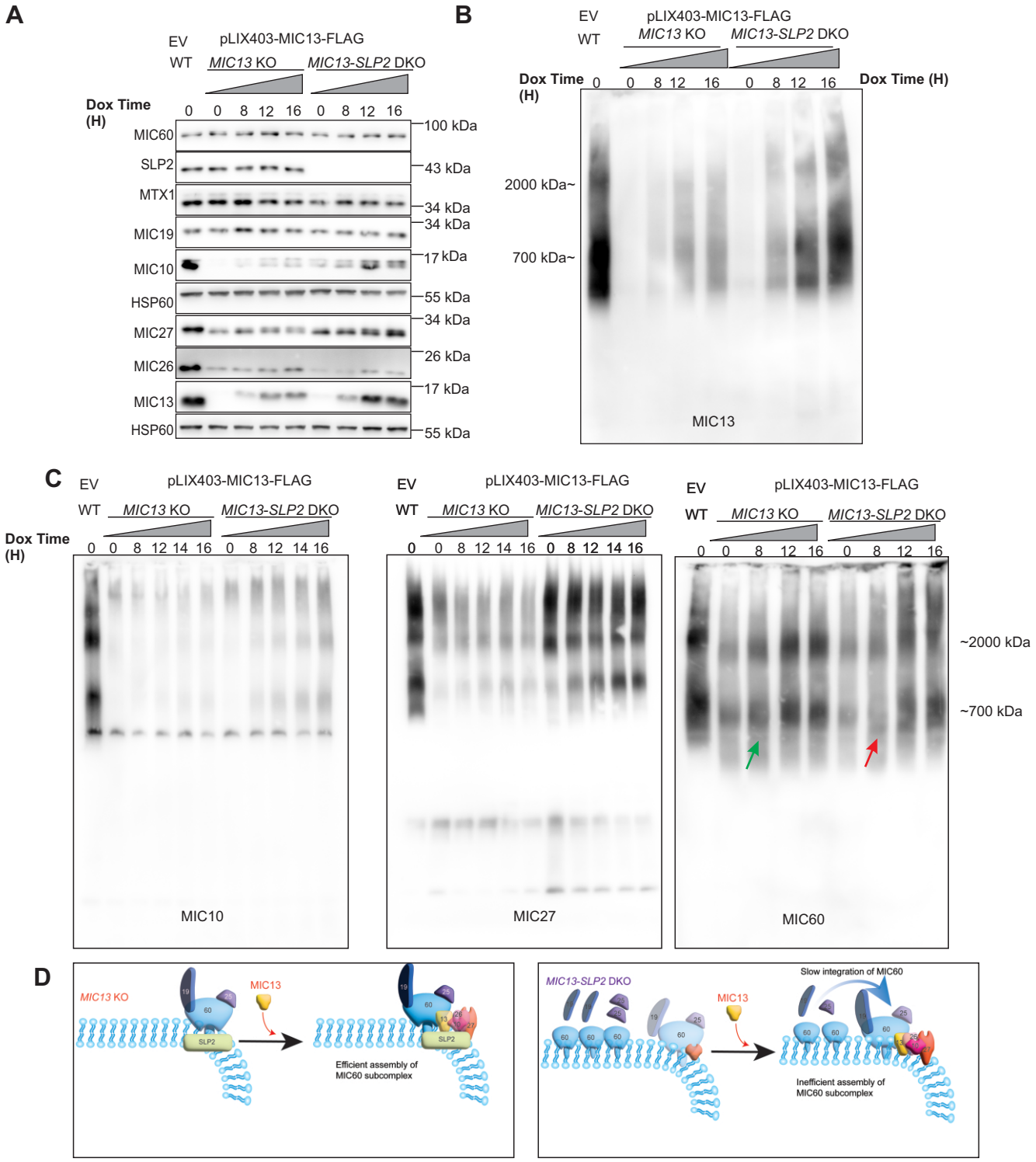

Figure 5. SLP2 regulates assembly kinetics of MIC60 in absence of MIC10-subcomplex

Figure 5. SLP2 specifically regulates assembly kinetics of MIC60 in the absence of MIC10-subcomplex. A, WT cells stably expressing pLIX403 EV and *MIC13* KO, *MIC13-SLP2* DKO cells stably expressing pLIX403-MIC13-FLAG were treated with 1 µg/ml of doxycycline (Dox) for indicated time points and western blot analysis depicting steady state levels of MICOS proteins upon induction of MIC13-FLAG are shown. **B,** BN-PAGE with isolated mitochondria from WT cells stably expressing pLIX403 EV, and *MIC13* KO and *MIC13-SLP2 DKO* cells stably expressing pLIX403-MIC13-FLAG treated with 1 µg/ml of doxycycline (Dox) for indicated time points showing stable incorporation of MIC13-FLAG in MICOS complex. **C,** Blue native PAGE with isolated mitochondria from WT cells stably expressing pLIX403 EV, and *MIC13* KO and *MIC13-SLP2 DKO* cells stably expressing pLIX403-MIC13-FLAG treated with 1 µg/ml of Dox for indicated time points was probed for MIC10, MIC27 and MIC60 antibody. It shows that kinetics of MIC60 assembly was dependent on SLP2. **D,** A model depicting the assembly kinetics of MIC60 in MICOS complex depends on SLP2.

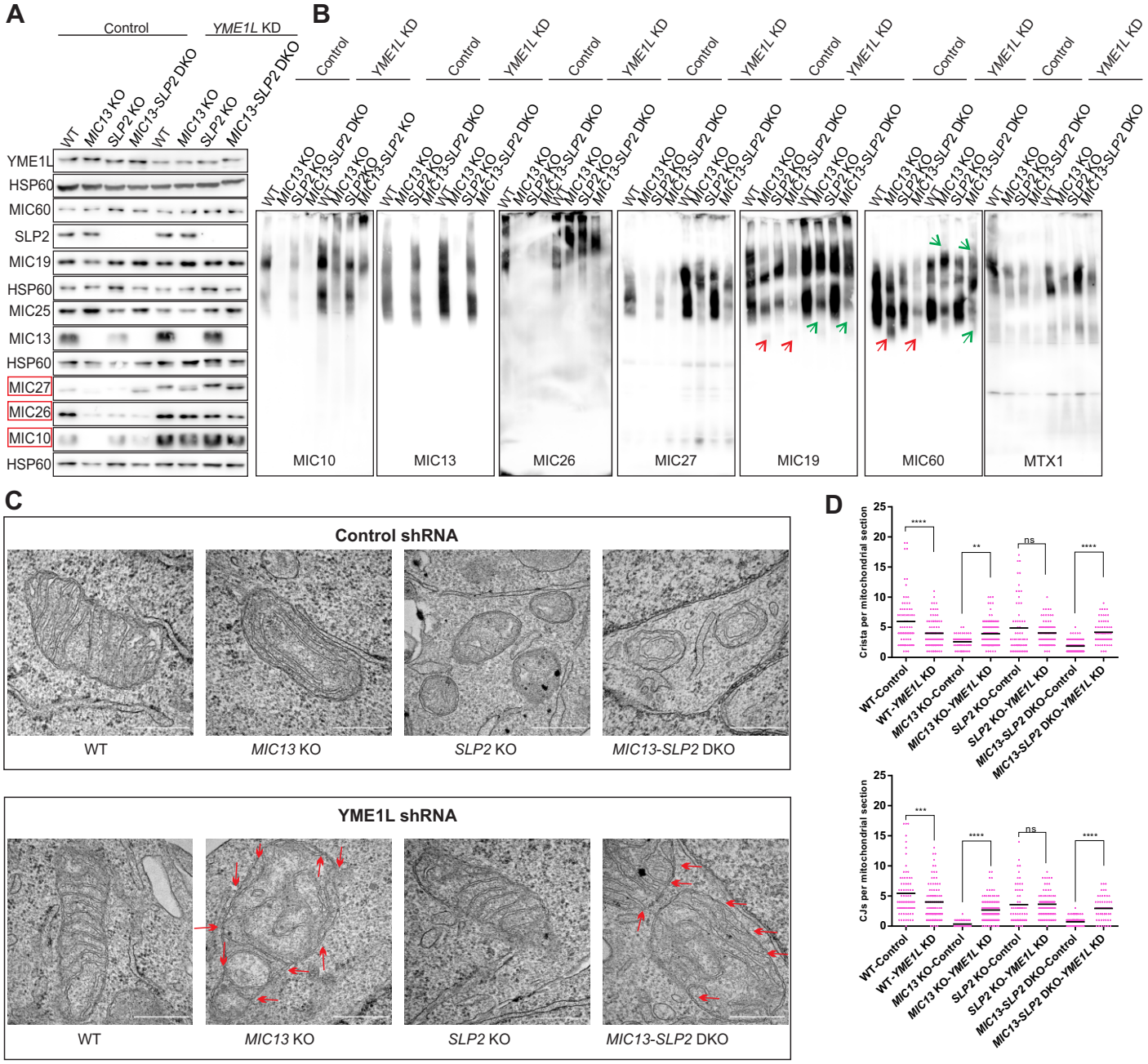

Figure 6. MIC13-YME1L and SLP2-YME1L axes stabilize MIC10- and MIC60-subcomplex assembly in a co-dependent manner

Figure 6. MIC13-YME1L and SLP2-YME1L axes stabilize MIC10- and MIC60-subcomplex assembly in a co-dependent manner. A, WT, *MIC13* KO, *SLP2* KO, *MIC13-SLP2* DKO stably expressing pGIPZ-Control shRNA or pGIPZ-YME1L shRNA (knockdown represented as KD) subjected to western blot to assess steady state levels of MICOS proteins. The levels of MIC10, MIC26 and MIC27 were dependent on YME1L-mediated proteolysis. **B,** BN-PAGE with isolated mitochondria from WT, *MIC13* KO, *SLP2* KO, *MIC13-SLP2 DKO* stably expressing pGIPZ-Control shRNA or pGIPZ- YME1L shRNA. Red arrow indicates downshift of MIC60 and green arrow indicates upshift of MIC60 in BN-PAGE. **C,** Mitochondrial cristae morphology accessed using TEM from WT, *MIC13* KO, *SLP2* KO, *MIC13-SLP2* DKO stably expressing pGIPZ-Control shRNA or pGIPZ-YME1L shRNA. Scale bar represents 0.5 µm. Red arrows depicts CJs rescue upon YME1L depletion in *MIC13* KO or *MIC13-SLP2* DKO cells. **D,** Quantification of crista and CJs per mitochondrial section. Outliers were removed with Grubbs' method and statistical significance was analysed by one-way ANOVA. *P-value ≤ 0.05, **P-value ≤ 0.01, ***P-value ≤ 0.001.

A

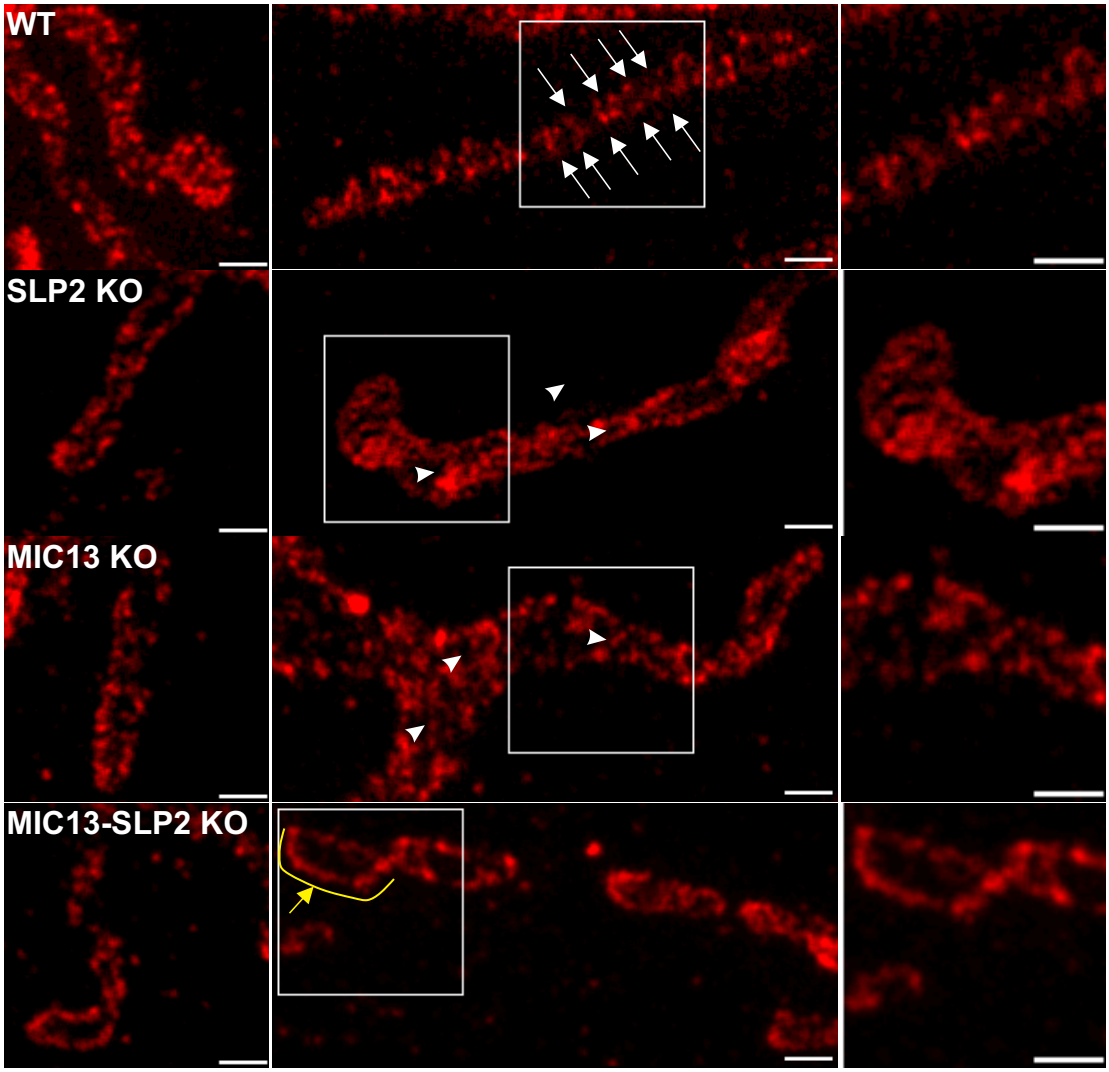

B

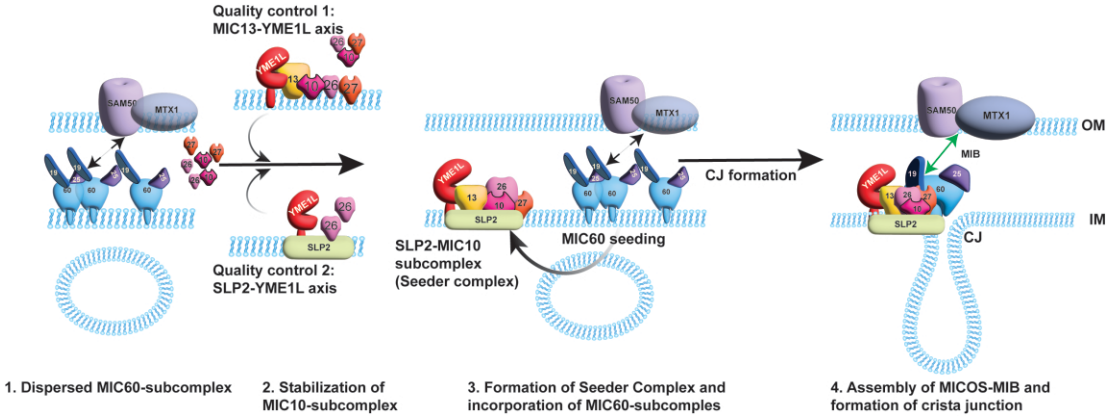

Figure 7. MIC13-SLP2 axis is required for formation of MIC60 punctae

Figure 7. MIC13-SLP2 axis is required for formation of MIC60 punctae. **A,** STED nanoscopy images from WT, *MIC13* KO, *SLP2* KO and *MIC13-SLP2 DKO* cells displaying MIC60 punctae. White arrows indicate individual MIC60 punctae in a rail -like arrangement in WT cells. Arrow heads depict perturbed MIC60 punctae in *MIC13* KO and *SLP2* KO. Yellow arrow with curve depicts dispersed MIC60 punctae in *MIC13-SLP2* DKO cells. **B,** A comprehensive schematic model of cristae junction morphogenesis illustrating the novel quality control process orchestrated by the MIC13 -YME1L and SLP2-YME1L axis, which facilitates the formation of the SLP2 -MIC10-subcomplex, known as the "seeder complex." This seeder complex serves as a pivotal catalyst for the subsequent assembly of the MIC60 subcomplex and the essential MIB protein MTX1, consequently playing a crucial role in defining the formation of MIC60 puncta and the MICOS-MIB complex, which promotes the establishment of cristae junctions within the mitochondrial structure.